Title

The role of surface forces in environment-enhanced cracking of brittle solids

Authors

Eskandari-Ghadi, Mehdi
Nakagawa, Seiji
Deng, Hang
et al.

Publication Date

2023-03-01

DOI

10.1016/j.jmps.2022.105162

The role of surface forces in environment-enhanced cracking of brittle solids

Mehdi Eskandari-Ghadi[1], Seiji Nakagawa[2], Hang Deng[2], Steve Pride[2], Benjamin Gilbert[2], Yida Zhang[1]

ABSTRACT

Fracture initiation and propagation in brittle materials is promoted in surface-reactive (sorptive) environments, a phenomenon known as subcritical crack growth (SCG). Laboratory measured crack-propagation velocity vs. stress intensity factor relationships typically exhibit highly nonlinear, multi-stage characteristics that are sensitive to environmental factors such as adsorbate concentration and temperature. For practical purposes, empirical relationships (e.g., a power law) have been used to describe this complex phenomenon. However, how the overall SCG behavior emerges from the underlying fundamental processes near the crack tip, such as the interaction of the crack surfaces separated by only a few nanometers and mass transport within the nano-confined space, is still not well understood. This paper develops a mechanistic, surface-force-based fracture theory (SFFT) which integrates surface force models, fluid transport models, and linear elastic fracture mechanics to quantitatively explain the multi-stage characteristics of SCG in brittle solids. A numerical model is developed based on SFFT and solved through an implicit partitioned scheme for efficiency and modularity. The results are validated by Wiederhorn's data on crack propagation in soda-lime glasses at a wide range of relative humidity levels. We show that, for the first time, the entire range of an SCG curve can be captured by a single physics-based model. The predicted SCG curves reveal that the development of repulsive disjoining pressure behind the crack tip can be responsible for the reduced apparent fracture toughness in a sorptive environment. The shape of the SCG curve, and its changes with respect to the environment, is found to critically depend on the assumed transport models.

Key words: fracture, kinetics, subcritical crack growth, surface force, sorption.

---

[1] *Department of Civil, Environmental and Architectural Engineering, University of Colorado Boulder, Boulder, CO*
[2] *Lawrence Berkeley National Laboratory, Berkeley, CA*
* *Corresponding author, E-mail address:* yida.zhang@colorado.edu

1. BACKGROUND

Subcritical crack growth plays a crucial role in the long-term mechanical performance of natural and engineered materials. In sorptive environments, or as referred to by Rice (1978) the *surface-reactive* environments, stable crack growth with a finite velocity (v_c) can occur at stress intensity factors (K_I) significantly lower than the critical one (K_{IC}) measured under the apparent 'dry' or vacuum conditions. This phenomenon is known as subcritical crack growth (SCG) (Atkinson, 1982) or static fatigue (Charles, 1958). SCG controls the rate of important geological processes such as the diagenesis of granular rocks (Chester et al., 2007) and weathering (Eppes and Keanini, 2017). Because it can be viewed as a precursor to abrupt fracturing, understanding and modeling SCG can help improve the prediction of volcanic eruptions (Kilburn and Voight, 1998) and fault failure (Lennartz-Sassinek et al., 2014). SCG may also contribute to the slow degradation of engineering materials (such as concrete, glass, metal, sand, rock), which is important in civil and mechanical engineering practice (Freiman et al., 2009; Karimpour and Lade, 2010; Le et al., 2009; Simmons et al., 1978; Zhang and Buscarnera, 2018).

The key challenge of quantitative modeling of SCG is rooted in its nonlinear multistage behavior resulted from complex physiochemical interactions at various length scales. SCG typically exhibits three distinct stages in the $v_c - K_I$ space (Fig. 1a). At relatively low K_I (stage I), v_c increases rapidly with K_I due to solid-environment interactions; at intermediate K_I (stage II), v_c is believed to be controlled by the transport of the active species; stage II continues until a sudden and rapid increase of v_c (stage III) as K_I exceeds the intrinsic fracture threshold (K_{IC}) of the material in vacuum (Freiman et al., 2009; Wiederhorn, 1967). The stage I and II curves strongly depend on environmental conditions such as temperature and reactant (adsorbate) concentration in the environment (Fig. 1b) (Crichton et al., 1999; Wiederhorn et al., 1980). In this context, our SCG model aims to address two key questions: (Q1) how do solid and environment interact to cause the reduced fracture toughness (from K_{IC} to K_{I0} in Fig. 1a) and the associated exponential kinetics in stage I? and (Q2) what transport mechanism (or combination of mechanisms) is at work near the crack tip to effectively limit the crack velocity in stage II?

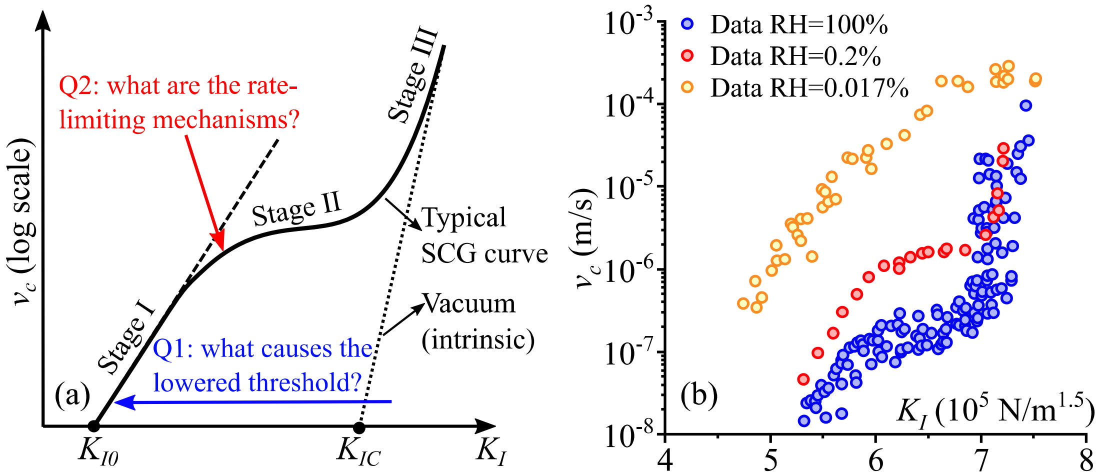

Fig. 1. (a) Typical SCG curve and the two fundamental questions. (b) SCG data of soda-lime glass at different relative humidity, RH (Wiederhorn, 1967; Wiederhorn et al., 1980).

Regarding the first question, many hypotheses have been proposed for different material-environment systems. Energy-based approaches explain the reduction of apparent fracture toughness through the decreased surface energy caused by the adsorption of fluid species on the crack surfaces (Rice, 1978; Wan et al., 1990). In contrast, atomistic approaches focus on crack-tip chemical reactions such as hydrolysis of stretched crack-tip bonds, dissolution and transport of crack tip material, and ion exchange with the crack tip (Atkinson, 1984; Michalske and Freiman, 1982). Concurrent with these mechanisms are the crack kinetic models by making analogy between crack propagation and reaction kinetics (Bazant and Planas, 1997; Lawn, 1975). Alternatively, empirical $v_c - K_I$ relationships such as power law are used as a descriptive tool without considering the underlying mechanisms driving the crack propagation (Bazant and Planas, 1997; Charles, 1958).

For the second question, some mechanisms such as Fickian diffusion (Wiederhorn, 1967), Knudsen diffusion (Lawn, 1974), and surface diffusion (Crichton et al., 1999) have been proposed to govern the fluid invasion along a crack. However, the temperature-dependence of SCG data observed in phosphate laser glasses suggests that none of these mechanisms alone can fully describe the stage II behavior (Crichton et al., 1999). Mass transport in nano-confined spaces is still an active area of research (Choi et al., 2001; Cihan et al., 2019) and is poorly understood at this moment for the near-crack-tip region. For these reasons, to this day, the modeling of stage II and the transition from stages I to II remains highly simplistic and phenomenological. Frequently, the stage II and III behaviors are neglected altogether, and only power-law relationships are fitted to the $v_c - K_I$ data obtained in stage I, across a range of stresses and environmental conditions (Brantut et al., 2013; Eppes et al., 2018; Nara et al., 2012; Olson, 1993).

Recently, atomic force microscope (AFM) and surface force apparatus (SFA) experiments revealed that repulsive forces (e.g., electrical double layer, hydration, crystallization) can become dominant between mineral surfaces at nanometer separations in the presence of sorptive species (Dziadkowiec et al., 2018; Røyne et al., 2015). Specifically, SFA measurements and molecular dynamic simulations (MD) suggest that the nano-confinement of solutions between calcite surfaces can exert repulsion over hundreds of nanometers of separation (Diao and Espinosa-Marzal, 2016; Dziadkowiec et al., 2019). AFM measurements confirm that forces of similar range exist between glass surfaces in aqueous solutions (Acuña and Toledo, 2008), and their magnitudes depend on the chemical composition of the environmental fluid (Adler et al., 2001). This inspires an alternative explanation of the complex SCG behavior: the repulsive forces along the crack walls can possibly facilitate the initiation and propagation of cracks in sorptive environments, resulting in the characteristic trend of an SCG curve in Fig. 1. Although the potential of surface forces in affecting solid fracture was debated in the glass community a few decades ago (Lawn, 1985; Wiederhorn and Fuller Jr, 1989), it has been largely neglected since then, without much progress.

2. A SURFACE-FORCE BASED FRACTURE THEORY

Provided the renewed evidence of repulsive surface forces induced by surface sorption, we propose an SCG theory to assess a mechanistic, surface-force-based answer to both questions. The key strategy is illustrated in Fig. 2 and explained in the following. In this model, surface forces along crack surfaces are accounted for via a force-separation relation. For a homogenous material in perfect vacuum, $\Pi(w)$ is defined by the force required to overcome the solid-solid intermolecular forces in separating two surfaces and is the same everywhere along the crack. The interacting force at different location x along the crack surface can be read from this $\Pi(w)$ curve given the local crack separation $w(x)$. The resistance against crack opening provided by the attractive surface force is macroscopically manifested as the fracture toughness K_{IC} in classical fracture mechanics (Meng and Thouless, 2019). This part is similar to the well-established cohesive crack theory (CCT), where the cohesive forces in the fracture process zone (FPZ) counterbalance the far-field tensile stress to give a net-zero stress intensity factor at the crack tip (Barenblatt, 1962).

Now consider that the crack is invaded by sorptive species, resulting in a non-uniform distribution of species concentration $C = C(x)$ along the crack as shown at the bottom of Fig. 2. Intrusion of the sorptive molecules can shift the local $\Pi(w)$ towards the repulsive side (Eskandari-Ghadi and Zhang, 2022), the magnitude of which depends on the local chemistry $C(x)$. The surface force at different locations therefore starts to travel along different $\Pi(w)$ curves as opposed to the vacuum case. The $C(x)$ profile is dictated by the species transportation along the crack and is thus coupled with the crack opening profile $w(x)$, the ambient concentration C_0, and the crack velocity v_c. The proposed theory can potentially explain the first question (Q1) through the reduced attraction or the development of repulsion due to the presence of sorptive species. The second question (Q2) can be also directly addressed through the coupling between fracture propagation and species transport in cracks.

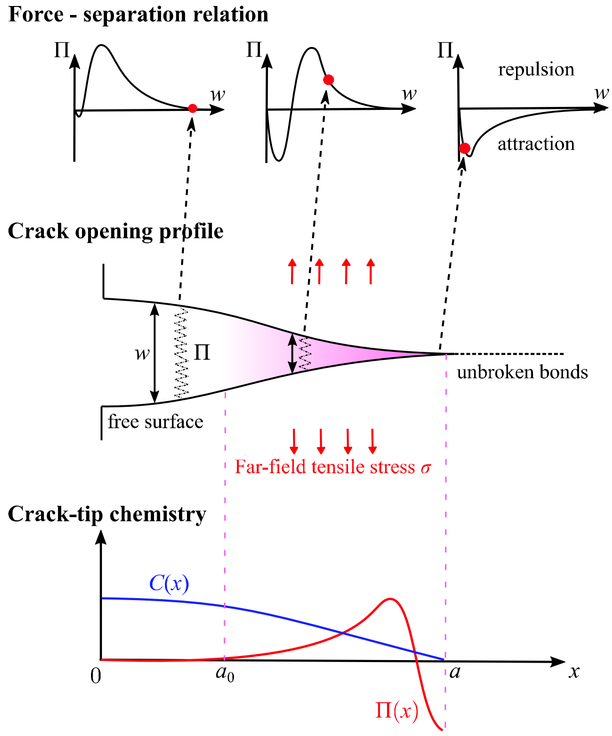

Fig. 2. The key elements of the proposed surface-force based fracture theory.

The proposed theory operates at an intermediate scale which is larger than the atomistic theories without relying on the dynamics of the crack-tip bond but is smaller than the macroscopic energy approaches by requiring the full resolution of crack opening profile and stress fields near the crack tip. It also differs from the cohesive crack theory in that, the traction curve in CCT is a constitutive relation commonly fitted to macroscale fracture testing data, involving only attractive force, and does not vary along the crack. In contrast, the proposed approach is rooted in surface physics, involves intermediate-scale force-separation relationships which are either directly measurable by SFA experiments or theoretically derivable based on intermolecular potentials, and can be strongly repulsive and vary with the local environment. We therefore refer to the proposed theoretical framework as the Surface-Force based Fracture Theory (SFFT) to distinguish from the previous works.

The remainder of this paper shall tackle two specific goals: (1) to formalize the mathematical structure of SFFT for mode-I fractures and (2) to numerically implement an SFFT model and test its ability in capturing typical SCG behaviors. For demonstration, the model will be specialized for the glass-in-vapor experiments of Wiederhorn (1967) as our first step towards advancing our general understanding of environment-enhanced cracking of brittle materials. We start by laying out the stress intensity, opening profile, and propagation kinetics of cracks with considering both far-field stress and distributed stresses along the crack surface (Section 3). We then formulate simplified analytical models for surface force under variable environment (Section 4) and species transport along a moving non-parallel slit (i.e., a propagating crack) (Section 5). We numerically solve the system via a partitioned implicit scheme to ensure a robust and efficient coupling between the aforementioned processes (Section 6). Finally, the model performance is assessed using the SCG data of soda-lime glass at different humidity levels as presented in Fig. 1b (Section 7). The main conclusions and possible future extensions of this work are discussed at the end (Section 8).

3. FRACTURE MODELING CONSIDERING SURFACE FORCES

3.1. Fracture mechanics analysis

We adopt the approach of Lawn (1985) by directly acknowledging the disjoining pressure (Π) in the LEFM analysis. The *disjoining pressure* Π is here defined as the net surface force between two solid surfaces normalized by the surface area (Clarke et al., 1986). It lumps the contributions of all solid-fluid interactions together without discerning their physiochemical origins and takes a positive value when the net force is repulsive (or disjoining) and negative when cohesive (or joining). Such distributed pressure along the crack surface can alter the stress field, characterized by the *effective* stress intensity factor (K_{Ie}), in the vicinity of the crack tip. K_{Ie} should be distinguished from the applied stress intensity (K_{Ia}) which solely accounts for the external forces or far-field stresses on the cracked solid.

Let us consider a 2D (plane-strain) edge crack of finite length a (Fig. 3a) in an elastic half-space subject to far-field tensile stress and disjoining pressure $\Pi(x)$ over the crack surface. The boundary conditions are selected such that the problem is equivalent to an infinite body with a line crack (Irwin, 1957) (Fig. 3b). This allows one to take advantage of the readily available fundamental solutions to calculate the mode-I crack opening and stress intensity under various loading combinations (Tada et al., 2000). The dependency of $\Pi(x)$ on fluid chemistry and species transportation will be addressed in section 4.

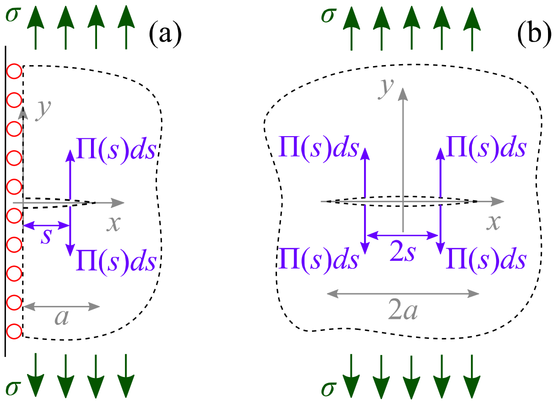

Fig. 3. Schematic of the model geometry and loading scenarios. (a) A finite edge crack in semi-infinite elastic domain. (b) A finite center crack in elastic infinite domain. The boundary conditions in (a) guarantee equivalent stress-deformation solution as (b).

LEFM allows one to write the effective stress intensity factor in an additive fashion

$$K_{Ie} = \underbrace{k_{I\sigma}\sigma}_{K_{Ia}} + \underbrace{\int_{s=0}^{s=a} k_{I\Pi}(s)\Pi(w(s);s)ds}_{K_{I\Pi}} \qquad (1)$$

where $k_{I\sigma}$ is the stress intensity factor caused by unit far-field tensile stress; σ is the magnitude of the tensile stress; $k_{I\Pi}(s)$ is the stress intensity factor caused by unit repulsive force on the crack surface at location s; $w(x)$ is the crack opening at location x; $\Pi(w)$ describes a disjoining pressure vs. separation relation which will be given by the surface force model (see Section 4); K_{Ia} is the applied stress intensity factor; $K_{I\Pi}$ is the stress intensity contribution by the disjoining pressure and takes a negative value when the net effect of Π is cohesive.

For a given σ, the distribution $\Pi(x) = \Pi(w(x); x)$ is not known a priori. Π depends on the surface separation while its change in turn alters the crack opening profile. The expression of $w(x)$ is given below based on LEFM (Bazant and Planas, 1997):

$$w(x) = c_{\sigma}(x)\sigma + \int_{s=0}^{s=a} c_{\Pi}(x,s)\Pi(w(s);s)ds \tag{2}$$

where $c_{\sigma}(x)$ is the crack opening at location x along the crack caused by unit far-field tensile stress; $c_{\Pi}(x,s)$ is the crack opening at the same location caused by a unit repulsive force at location s.

For the geometry sketched in Fig. 3a and b, $k_{I\sigma}$ and $c_{\sigma}(x)$ are given by Tada et al. (2000)

$$k_{I\sigma} = \sqrt{\pi a} \text{ and } c_{\sigma}(x) = \frac{4(1-\nu^2)}{E}\sqrt{a^2 - x^2} \tag{3}$$

Similar fundamental solutions can be found for unit surface force applied at s:

$$c_{\Pi}(x,s) = \frac{8(1-\nu^2)}{\pi E}\begin{cases} \tanh^{-1}\sqrt{\dfrac{a^2-s^2}{a^2-x^2}} & ; \quad x < s \\ \coth^{-1}\sqrt{\dfrac{a^2-s^2}{a^2-x^2}} & ; \quad x > s \end{cases} \tag{4}$$

$$k_{I\Pi}(s) = 2\sqrt{\frac{a}{\pi}}\frac{1}{\sqrt{a^2 - s^2}} \tag{5}$$

It should be noted that Eqns. (4) and (5) are singular at $x = s$. This introduces difficulties to the numerical integrations of Eqns. (1) and (2). We have circumvented this difficulty by means of numerical approximation which allows the usage of non-singular analytical solutions (see Appendix A for details).

The non-linear coupling between $w(x)$ and $\Pi(w)$ can be assembled as a system of two algebraic equations, referred to as the $\Pi - w$ system hereafter, to be solved simultaneously (see Appendix A). The solution to the $\Pi - w$ system provides a crack opening profile $w(x)$ which will be substituted into Eq. (1) in conjunction with the $\Pi(w)$ model (see Section 4) to obtain K_{Ie}.

3.2. Crack propagation kinetics

The rate at which crack propagates can be studied in the framework of reaction rate theory (Charles, 1962). Griffith's criterion suggests that non-dissipative crack propagation occurs once $(\mathbf{G} - 2\gamma) > 0$, where $\mathbf{G}$ is known as the energy release rate and γ is the surface tension of the newly created crack faces. By analyzing the statistics of bond breakage and healing under the energy difference $(\mathbf{G} - 2\gamma)$ in a way similar to a chemical reaction driven by chemical potential differences (Lawn, 1975), one can arrive at the following kinetic equation

$$v_c = v_0 \exp\left(-\frac{Q_0}{RT}\right) \sinh\left(\frac{\tilde{\kappa}_0 (\mathbf{G} - 2\gamma)}{RT}\right) \tag{6}$$

where $\tilde{\kappa}_0$ is a proportionality factor; Q_0 is the activation energy for bond breaking; v_0 contains information of the solid lattice vibration frequency and lattice length-scale (Meng and Thouless, 2019). In Eq. (6), the "driving force" for crack propagation is $(\mathbf{G} - 2\gamma)$. Bazant and Planas (1997) have shown that stress intensity factor can be also taken as the driving force to replace $(\mathbf{G} - 2\gamma)$ in Eq. (6). Inspired by this, we propose a slightly different equation for crack growth in the presence of disjoining pressure

$$v_c = v_0 \exp\left(-\frac{Q_0}{RT}\right) \sinh\left(\frac{\kappa_0 K_{Ie}}{RT}\right) \tag{7}$$

where κ_0 is a proportionality factor related to $\tilde{\kappa}_0$. The decomposition of K_{Ie} to K_{Ia} and $K_{I\Pi}$ (i.e., Eq. (1)) reveals some connections between Eqns. (6) and (7). Firstly, the celebrated Irwin equation directly links K_{Ia} and $K_{I\Pi}$, respectively, to $\mathbf{G}$ and 2γ at equilibrium. $K_{Ie}=0$ implies that $\mathbf{G}=2\gamma$ and $v_c=0$, agreeing that a non-propagating crack attains zero stress intensity and thus finite tensile stress at the tip (Barenblatt, 1962). Secondly, the generation of repulsive disjoining pressure in sorptive environment will reduce $K_{I\Pi}$ (Eq. (1)), thus promoting crack propagation under the same applied K_{Ia}. This is equivalent to the surface energy reduction mechanism discussed by Rice (1978). We further argue that Eq. (7) has the unique advantage of directly incorporating the nonuniform reduction of surface energy along the crack (via $K_{I\Pi}$) caused by transient processes such as fluid transport, the inclusion of which in energy-based descriptions is not straightforward.

4. SURFACE FORCE MODEL

The magnitudes of surface forces depend on the crack aperture w (Bazant and Planas, 1997) as well as the local environment C (Israelachvili, 2011). The net effect of these forces over unit surface area can be collectively encapsulated in the disjoining pressure $\Pi(w,C)$, the modeling of which is essential for the proposed fracture theory. Before tackling this task, we should clarify the ambiguity related to the definition of "crack tip".

From an atomistic perspective, the crack tip may be defined at the location where the solid chemical bonds are broken. Thermodynamically, one may define the crack tip as the point behind which the separation of opposite surfaces is irreversible and involves energy dissipation, and in front of which the separation occurs reversibly or elastically. Indeed, the location of the "crack tip" behind and ahead of which different inelastic processes may be at work is only a matter of perspective and convenience (Sills and Thouless, 2015). From a continuum point of view, undamaged material obeys elastic behavior, and the damaged material in the fracture process zone (FPZ) obeys a softening stress-strain relation (Bažant and Oh, 1983). The point of divergence between continuum and localized crack happens at the maximum value of traction on the force-separation curve. This motivates us to define the crack tip as the point of maximum traction between two surfaces, and the corresponding crack separation at this reference point is taken as $w = 0$ (See Fig. 4).

The consideration of purely cohesive interactions (traction) over several micrometers behind crack tip leads to the well-known cohesive crack theory. It has been successfully applied, for example, to remove the stress singularity predicted by LEFM at the crack tip (Barenblatt, 1962), model the kinetics of crack growth (Meng and Thouless, 2019), and capture crack fatigue (Allegri, 2020; Nguyen et al., 2001). It also hosts various material-specific fracture models by treating the traction-separation curve as a constitutive relation (Hillerborg et al., 1976; MAI and Lawn, 1987; Needleman, 1990; Tijssens et al., 2000; Tvergaard and Hutchinson, 1992). However, the true surface forces originated from the physical separation (<100 nm) of solid surfaces (electrostatic, van der Waals, etc.) and environmental attack (surface hydration, electrical double layer, etc.) has been mostly neglected in classical fracture analysis. The goal here is to substantialize a $\Pi(w, C)$ model to capture these nanometer-scale interactions which can be attractive or repulsive.

Generally, the disjoining pressure between two solid surfaces in arbitrary environment can be decomposed into two contributions:

$$\Pi(w, C) = \Pi_0(w) + \Delta\Pi(w, C) \tag{8}$$

where C stands for the concentration of the sorptive species in between surfaces. C could be generalized to a vector $\mathbf{C} = [C_1, C_2, \ldots, C_k]$ should multiple sorptive species present in the environment. The first component, Π_0, accounts for the intrinsic surface forces between two solid surfaces in vacuum; the second term, $\Delta\Pi$, collects the change of disjoining pressure due to solid-species interaction (Adapa and Malani, 2021; Dziadkowiec et al., 2018; Røyne et al., 2015).

4.1. Surface force in vacuum $\Pi_0(w)$

$\Pi_0(w)$ may be constructed through smooth interpolations of experimental data provided by SFA/AFM measurements, or rigorously derived with the knowledge of the total intermolecular pair potentials of the solid (Israelachvili, 2011). Here we opt for a well-behaved and versatile analytical expression to represent the in-vacuum surface forces of generic materials. Simple analytical models also benefit the numerical implementation in terms of both convergence and efficiency. A two-parameter equation is adopted for this purpose:

$$\Pi_0 = -\Pi_{0,\max} \frac{w+w_0}{w_0} \exp\left(1-\frac{w+w_0}{w_0}\right) \tag{9}$$

where Π_0 attains maximum attraction $\Pi_{0,\max}$ at $w=0$ and decays exponentially for $w>0$, the rate of which is controlled by w_0. Eq. (9) also contains an exponentially increasing repulsive branch for $w<0$, which physically corresponds to the steric repulsion when molecules are brought too close together (Israelachvili, 2011). This feature is also expected to be numerically beneficial by serving as a penalty contact to avoid the overlap of two surfaces when they come to contact, in cases where crack healing may occur (i.e., $K_{Ie} < 0$). Eq. (9) is visualized in Fig. 4 for three sets of parameters.

The solution of Eqns. (2) and (9) together allows us to study crack opening at different levels of applied far-field stress in vacuum. Using the numerical method detailed later in Section 6 and parameters in Table 1, the w and Π_0 profiles for a crack of length 36mm under increasing stresses are plotted in Fig. 5. When the stress is low, the in-vacuum surface force contribution of stress intensity $K_{I\Pi}$ can effectively balance out the applied stress intensity K_{Ia}, thus gives a low K_{Ie} value and a near-equilibrium crack per Eq. (7). This results in a smoothly converging crack tip profile (the solid blue curve in Fig. 5a). This is consistent with Barenblatt (1962) who analytically showed that the crack opening profile in the immediate vicinity of the crack tip becomes proportional to the 1.5 power of the distance from the crack tip when $K_{Ic} \rightarrow 0$ (the dashed cyan curve). As the applied force increases, the crack is perturbed further away from equilibrium, and its tip geometry becomes blunt and approaches an elliptical shape. Besides the near-tip region, the overall crack opening profile (Fig. 5b) does not vary significantly for the range of applied σ, except for a proportional widening of the crack with increasing σ. Fig. 5c shows that the resultant Π_0 increasingly concentrates at the crack tip as the applied stress increases and the crack aperture widens up.

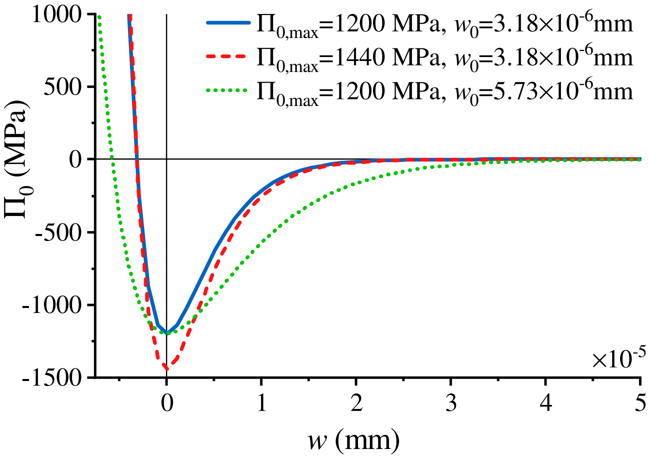

Fig. 4. The in-vacuum surface force described by Eq. (9). $\Pi_{0,\max}$ controls the magnitude of Π_0 while w_0 controls its spread along w.

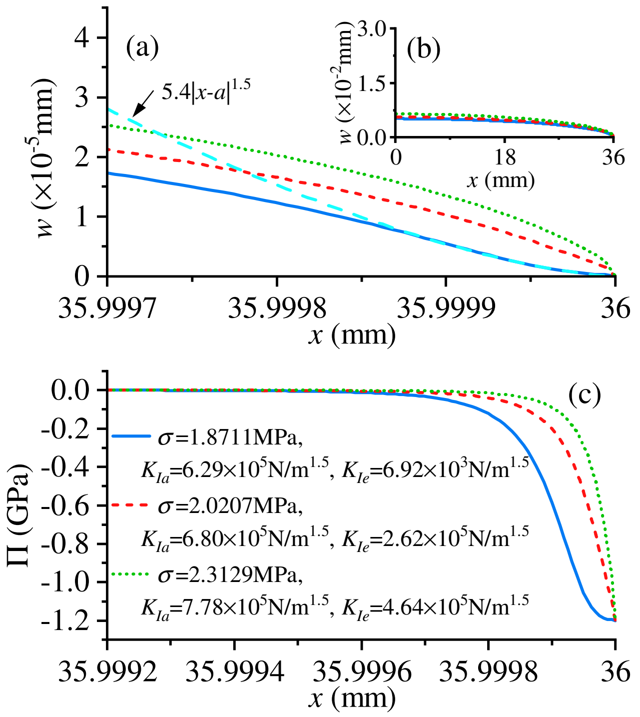

Fig. 5. The computed (a) crack tip opening profile, (b) overall crack opening profile, and (c) disjoining pressure distribution in vacuum for progressively increasing far-field tensile stress. The model parameters used here are listed in Table 1.

Figures 6a and 6b plot the computed K_{Ie} and $K_{I\Pi}$ against a wide range of applied K_{Ia} using the same parameters as Fig. 5. As expected, the presence of cohesive forces results in a reduced K_{Ie} compared to K_{Ia}. Increasing K_{Ia} results in a decrease of $K_{I\Pi}$ (Fig. 6b), and thus K_{Ie} asymptotes towards K_{Ia} (Fig. 6a). Lawn (1985) analytically derived an expression of $K_{I\Pi}$ as $K_{I\Pi} = -E'\gamma / K_{Ie}$, where $E' = E/(1-\nu^2)$ for plane-strain, by neglecting the dependence of crack opening profile on Π_0. For the selected parameters, this approximation is surprisingly accurate for large K_{Ia} values but deviates from our exact solution of the full $\Pi - w$ system at lower K_{Ia} levels (Fig. 6b). This implies that the consideration of the two-way coupling between Π and w is essential for studying the onset of SCG which always occurs at low K_{Ia} values. Fig. 6c shows that $K_{I\Pi}^2 / E'$ asymptotes to 2γ as equilibrium ($K_{Ie} = 0$) is approached. This further supports our arguments that Eq. (7) can be viewed as the mechanistic counterpart to Eq. (6), and the Irwin's equation respectively links K_{Ia} and $K_{I\Pi}$ to $\mathbf{G}$ and 2γ at equilibrium.

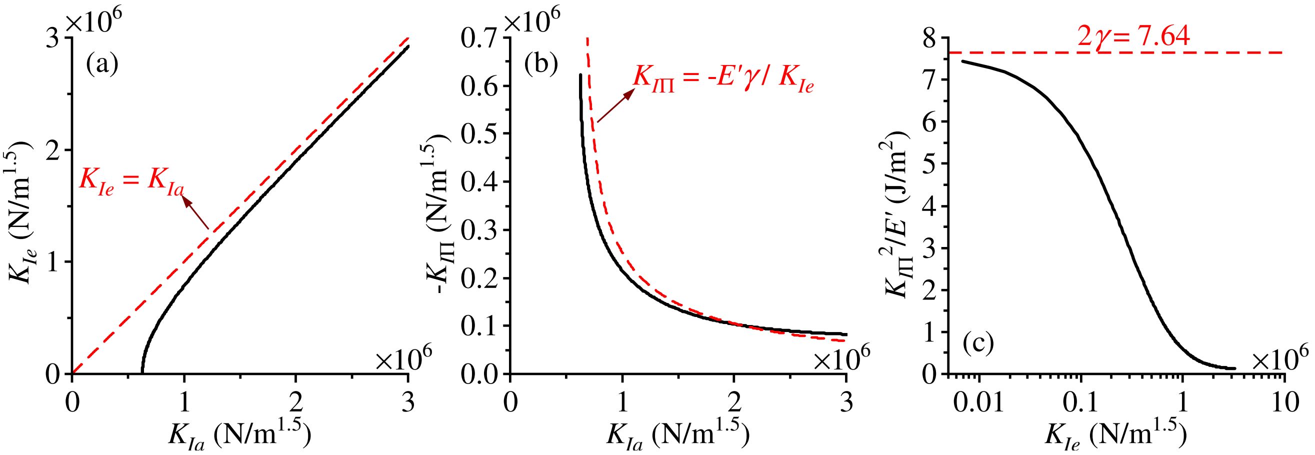

Fig. 6. Solutions of the $\Pi - w$ system in terms of (a) K_{Ie} versus K_{Ia} to compare with the prediction by Lawn (1985); (b) $-K_{I\Pi}$ versus K_{Ia} to compare with the approximate analysis by Lawn (1985); and $K_{I\Pi}^2 / E'$ versus K_{Ie} to study the application of Irwin's equation in linking $K_{I\Pi}^2 / E'$ and 2γ at equilibrium. E' is the elastic constant and equal to $E/(1-\nu^2)$ for plane strain condition. Parameters used are summarized in Table 1,

4.2. Induced disjoining pressure $\Delta\Pi$

The magnitude of $\Delta\Pi$ depends on both the surface separation w as well as the local concentration of sorptive species C (Adler et al., 2001; Eskandari-Ghadi and Zhang, 2021). To construct a $\Delta\Pi$ model, let us focus the discussion on Wiederhorn (1967)'s glass-in-vapor system from hereon. Particularly, we consider a single mode-I crack propagation in soda-lime glass in gaseous nitrogen at 25° with variable relative humidity. The relevant chemistry along the crack can be straightforwardly characterized by the partial pressure of the water vapor p . In this setting, the environment-induced disjoining pressure can be expressed by $\Delta\Pi(w, p)$. Note that we did not consider $\Delta\Pi$ as a function of time in this first treatment. In other words, we have assumed that the adsorption kinetics is much faster than the rate of subcritical crack propagation (< 10^{-4} m/s), and the only rate-limiting step in generating the repulsive disjoining pressure $\Delta\Pi$ is the transport of water vapor along the crack, as described by the transport models detailed in the next section.

Physically, many molecular-scale mechanisms can lead to the generation of $\Delta\Pi$ at various vapor pressures (Clarke et al., 1986). It is believed that these mechanisms mainly have origins in Van der Waals, electric double layer, and hydration forces, with the hydration force being the dominant contribution (Dziadkowiec, 2019). The exhaustive discussion of each of them is beyond the scope of this work. A smooth 4-parameter model is instead adopted for the environment-induced disjoining pressure:

$$\Delta\Pi(w,p)=f_{\Delta\Pi}(w)g_{\Delta\Pi}(p) \tag{10}$$

where

$$f_{\Delta\Pi}(w)=\begin{cases}\Delta\Pi_{\max}\dfrac{w+\tilde{w}_0}{\tilde{w}_0}\exp\left(1-\dfrac{w+\tilde{w}_0}{\tilde{w}_0}\right) & ;\ w\geq 0\\ f_{\Delta\Pi}(0) & ;\ w<0\end{cases} \tag{11}$$

captures the dependency of $\Delta\Pi$ on w by taking similar form as Eq. (9); and

$$g_{\Delta\Pi}(p)=\left(\frac{p}{p_{sat}}\right)^{\alpha}\exp\left(\beta\left(1-\frac{p_{sat}}{p}\right)\right) \tag{12}$$

characterizes the dependency of $\Delta\Pi$ on the vapor pressure p. $\Delta\Pi_{\max}$, $\tilde{w}_0$, α, and β are model parameters; p_{sat} is the saturation vapor pressure. The $f_{\Delta\Pi}$ expression exhibits an overall exponential decay, which is consistent with expressions adopted for hydration forces (Dziadkowiec et al., 2018; Israelachvili, 2011). The expression of g is constructed to 1) monotonically increase with increasing water vapor pressure p, 2) smoothly increase from zero, and 3) contain parameters that control the pressure and the steepness of the steepest increase. The value of $f_{\Delta\Pi}$ in the range of $w<0$ is assigned to ensure the overall Π model is smooth at w=0. Eqns. (10), (11), (12) and the total Π from Eq. (8) are visualized in Fig. 7 for different levels of p/p_{sat} and values of model parameters. Fig. 7a shows that parameters $\Delta\Pi_{\max}$ and $\tilde{w}_0$, respectively and independently, control the spread of $\Delta\Pi$ over separation and its magnitude. Fig. 7b shows that the overall curvature of $g_{\Delta\Pi}$ decreases with increasing α and β. α also controls the curvature at very small p values, while the effect of β is less concerned with small p. The resultant $\Delta\Pi$ in Fig. 7c resembles the disjoining pressure sketched in Ash et al. (1973) and the one derived by Eskandari-Ghadi and Zhang (2021) based on the BDDT isotherm (Brunauer et al., 1940). The total Π in Fig. 7d can be compared with the conceptual sketch by Røyne et al. (2015) for calcite surfaces.

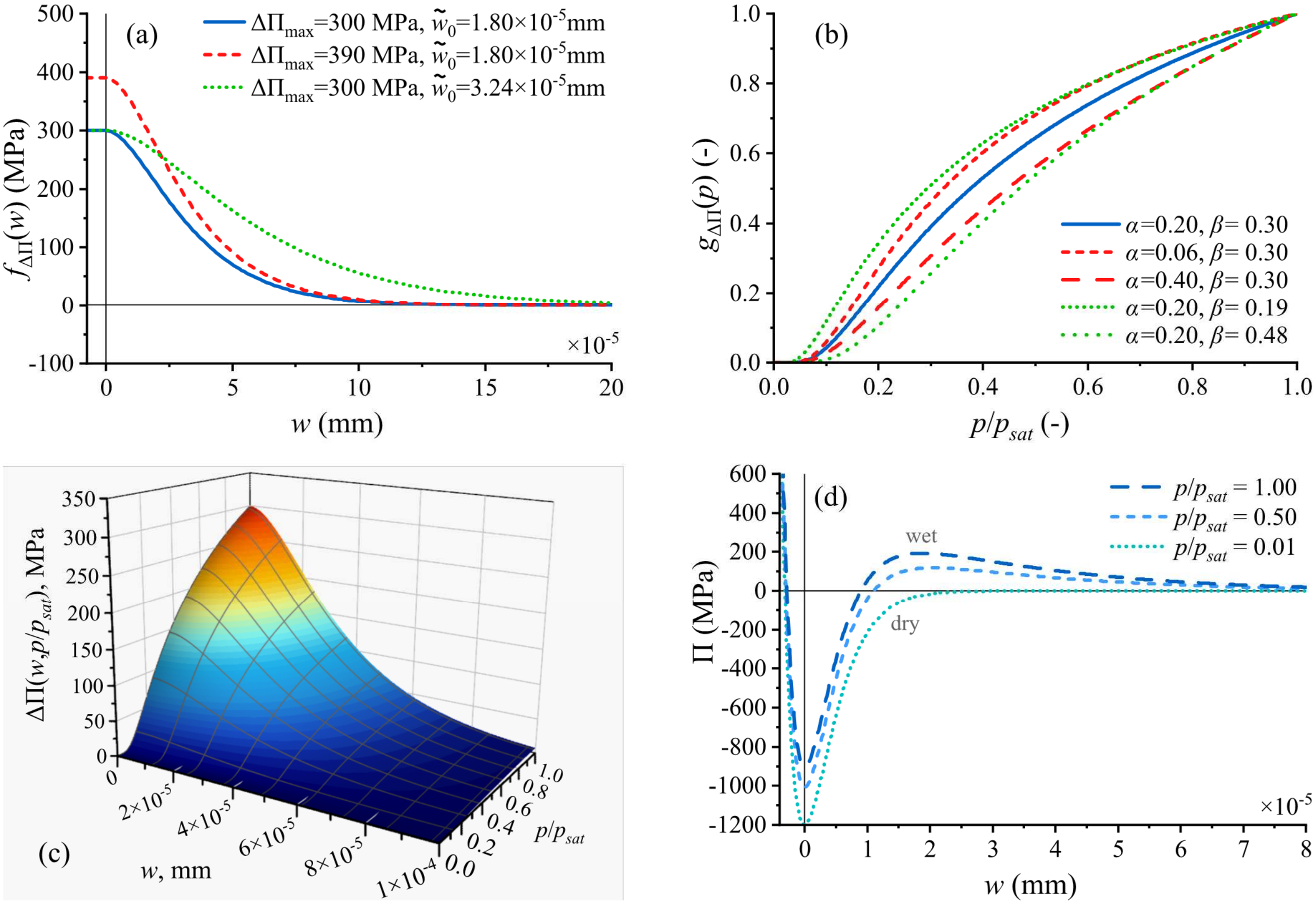

Fig. 7. Environment-induced disjoining pressure as a function of (a) separation and (b) relative partial pressure; (c) the $\Delta\Pi$ surface in the $w-p$ space with $\Delta\Pi_{\max}=300\text{MPa}$, $\tilde{w}_0=1.8\times10^{-5}\text{mm}$, $\alpha=0.2$, and $\beta=0.3$; and (d) the total disjoining pressure Eq. (8) with $\Pi_{0,\max}=1200\text{MPa}$ and $w_0=3.18\times10^{-6}\text{mm}$.

5. MASS TRANSPORT ALONG THE CRACK

The effect of sorption on crack growth is contingent upon the accessibility of sorptive species near the crack tip. This is controlled by the species transport along the crack path and is expected to trail behind as the crack propagates faster. The spatiotemporal evolution of species concentration in turn impacts the resultant disjoining pressure (Fig. 2) and further the K_{Ie} and the crack velocity, thus forming a two-way coupling. Resolving species transport is therefore essential to the proposed SFFT model for capturing the full SCG behavior. Below we develop a generic transport model to capture the most basic features of gas flow in cracks. A one-dimensional treatment is adopted, assuming that gas migrates towards the crack tip along the crack path (x-direction in Fig. 3a). The steady-state solution with respect to the crack tip of the transport model will be sought, considering crack propagation velocities in stages I and II are typically slow (of order 10^{-4} m/s or less). In other words, we examine the steady-state crack propagation scenarios at each K_{Ia} value during an SCG test without considering the short transient stages between K_{Ia} increments.

Consider a small segment δx along the crack with respect to the $x-y$ coordinate fixed in space (Fig. 8), the number of moles of sorptive species must be conserved:

$$\delta n(x,t)Lw(x)\delta x = J(x,t)Lw(x)\delta t - J(x+\delta x,t)Lw(x+\delta x)\delta t \tag{13}$$

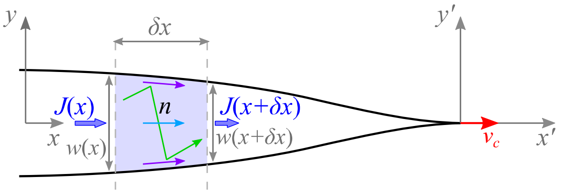

Fig. 8. Schematic of gas transport along propagating crack. The light blue, purple, and green arrows represent, respectively, bulk gas (viscous) flow, surface diffusion, and Knudsen flow as examples of the transport mechanisms.

where L is the depth of the crack in the z direction; n is the molar concentration with a unit of mole per volume; J is the molar flux with a unit of mole per unit area per unit time; and w is the crack opening treated here as a known. By Taylor expansion of $J(x+\delta x)$ and $w(x+\delta x)$, and taking the limit of $\delta x \to 0$ and $\delta t \to 0$, Eq. (13) can be rewritten as

$$\frac{\partial n(x,t)}{\partial t} = -\frac{1}{w(x,t)}\frac{\partial}{\partial x}\big(w(x,t)J(x,t)\big) \tag{14}$$

For an ever-expanding domain (i.e., a moving crack tip), "steady state" only makes sense for an observer that moves together with the crack tip, i.e., the near-tip species concentration profile stops evolving for that observer. Let us therefore define a new coordinate system $x' - y'$ that moves according to $x' = x - v_c t$ and $y' = y$ (Fig. 8). It follows $n_t(x,t) = n_t(x',t) - v_c n_{x'}(x',t)$ and $(w(x)J(x,t))_x = (w(x)J(x,t))_{x'}$, where $(\cdot)_t = \partial(\cdot)/\partial t$, $(\cdot)_x = \partial(\cdot)/\partial x$, and $(\cdot)_{x'} = \partial(\cdot)/\partial x'$. Thus the molar balance in Eq. (14) can be written in the $x' - y'$ coordinate as

$$\frac{\partial n(x',t)}{\partial t} = v_c \frac{\partial n(x',t)}{\partial x'} - \frac{1}{w(x',t)}\frac{\partial}{\partial x'}(w(x',t)J(x',t)) \tag{15}$$

Examining the steady-state condition $\partial(\cdot)/\partial t = 0$ of Eq. (15) gives the following ordinary differential equation:

$$v_c \frac{\partial n}{\partial x'} = \frac{1}{w}\frac{\partial}{\partial x'}(wJ) \tag{16}$$

It relates the steady-state profiles $n(x')$, $w(x')$, and $J(x')$ at given boundary conditions. Without losing generality, the species transport may be depicted by

$$J(x) = -D\frac{\partial n}{\partial x} \tag{17}$$

where D is a transport coefficient. At chemical equilibrium, the partial pressure (p), concentration (n), and chemical potential (μ) of the sorptive species are one-to-one related through the equation of state.

Thus, D can be re-written in terms of permeability for viscous and Knudsen flow or diffusivity for molecular and surface diffusion. This preserves the generality of the model and enables more detailed examinations of the various transport mechanisms in future studies. Substitution of Eq. (17) in Eq. (16) gives

$$v_c \frac{\partial p}{\partial x'} = -\frac{1}{w}\frac{\partial}{\partial x'}(wD\frac{\partial p}{\partial x'}) \tag{18}$$

where the ideal gas law ($p = nRT$) and isothermal process ($dT = 0$) are assumed. The steady-state pressure distribution $p(x')$ can be obtained by numerically solving Eq. (18) together with the $\Pi - w$ system introduced in the previous section. This is however numerically taxing considering solving the $\Pi - w$ system already requires an iterative scheme. Alternatively, an explicit analytical expression of $p(x')$ can be obtained by assuming $\partial w / \partial x' \approx 0$ and constant D in Eq. (18). This compromise significantly eases the global solution scheme and permits quantitative studies of the first-order behaviors of the proposed SFFT model. With these simplifying assumptions, Eq. (18) can be immediately integrated under the boundary conditions of $p = p_0$ at the crack mouth ($x' = -a$) and $J = v_c n$ at crack tip ($x' = 0$) to give:

$$p(x') = p_0 \exp\left(-\frac{v_c}{D}(x' + a) \right) \tag{19}$$

where p_0 is the partial gas pressure in the environment outside the crack.

In reality, it is expected that gas transport from crack mouth to tip involves multiple mechanisms each of which control the transport rate at different crack width (Fig. 9a). For example, bulk gas flow may be dominant at large crack openings (from M to A in Fig. 9b) because of the w^2-dependency of its diffusivity or permeability D (Wu et al., 2015). As the crack tip is approached and the crack opening narrows, viscous flow rapidly diminishes, and a secondary transport mechanism gains dominance to permit molecular diffusion in nanometer spaces (from B to T in Fig. 9b). This specific transport mechanism near crack tip is currently not well understood. Lawn (1974) argues that molecular collisions with the crack walls, known as Knudsen diffusion, is the mechanism of near-tip transport. Wiederhorn (1967) postulated that there exists a near-tip region, the so called "boundary layer", that is always inaccessible to bulk gas flow. Water molecules can only migrate through the gas mixture in this region via Fickian diffusion at the same rate that they are chemically consumed at the crack tip. Contrarily, experimental data from glass SCG at different temperatures by Crichton et al. (1999) does not support the dominance of Fickian diffusion nor Knudsen diffusion in the boundary layer by comparing the anticipated versus the observed temperature-dependence of the stage-II crack velocity. They suggested surface diffusion is a plausible mechanism to explain the temperature-dependence, but at the same time also suggested that more complex mechanisms or their combinations could be responsible. An ongoing research effort at the Lawrence Berkeley National Laboratory is aimed at providing better understanding of these complex transport mechanisms in glass cracks at nano-scale.

Given the lack of a comprehensive transport model that captures the various mechanisms along the crack, we opt for a simplified, segmented, analytical steady-state pressure profile to account for the multi-regime transport of species in complementary to the single-regime model in Eq. (19). Particularly, species transport is assumed to take form of rapid bulk flow for crack width $w > w_{th}$ (from M to C in Fig. 9c) where the pressure drop is negligible and slow diffusion for $w_{th} < w$ (from C to T in Fig. 9c) where the pressure profile is similarly described by Eq. (19):

$$\begin{cases} p(x') = p_0 & ; \quad \forall x' \mid w(x') > w_{th} \\ p(x') = p_0 \exp\left(-\frac{v_c}{D}(x' + d) \right) & ; \quad \forall x' \mid w(x') \leq w_{th} \end{cases} \tag{20}$$

where w_{th} is a threshold crack width to be discussed later; d is defined such that $w(x') > w_{th}$ for all $x' < -d$. This dual-regime model (Fig. 9c) is conceptually similar to Wiederhorn's boundary layer model (Wiederhorn, 1967). In essence, the only difference between the single-regime flow Eq. (19) and the dual-regime flow Eq. (20) is that d is fixed at $d = a$ in the former, but becomes a variable related to w_{th} in the latter.

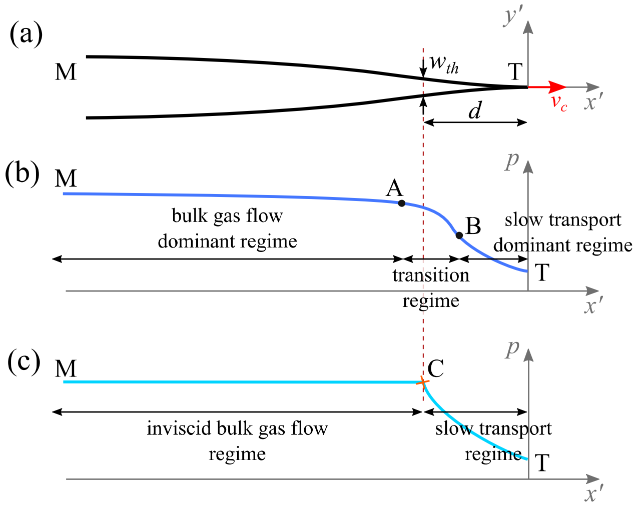

Fig. 9. Schematic of the near tip crack profile (a), the realistic pressure profile in nano-spaces (b) inspired by Cihan et al. (2021), and the approximated dual-regime pressure profile (c).

The threshold crack width w_{th} may be selected based on the Knudsen number, $\mathrm{Kn} = \lambda / w$, where λ is the mean free path of the gas (Lawn, 1974). $\mathrm{Kn} \ll 1$ suggests transport dominated by viscous flow, while $\mathrm{Kn} \gg 1$ suggests transport by slower diffusion mechanisms (Choi et al., 2001). Therefore, it is reasonable to define $w_{th} = \lambda / \mathrm{Kn}_0$ where Kn_0 marks the transition point taken to be $1/3$ here, well within the range of $0.01 < \mathrm{Kn}_0 < 1$ recommended by Lawn (1974). The experiments of glass SCG by Wiederhorn (1967) is performed in a nitrogen-water vapor environment at room temperature and atmospheric pressure, based on which the mean free path can be approximated as $\lambda \approx 7 \times 10^{-8}\,\mathrm{m}$ (Bird et al., 2006; Chapman and Cowling, 1990; Jennings, 1988).

Fig. 10a and b plot the steady-state vapor pressure profiles at different crack velocity for crack length $a = 36\text{mm}$ and ambient humidity $\mathrm{RH}_0 = p_0 / p_{sat} = 0.3$. The dual-regime flow based on the current estimation of w_{th} predicts that the slow molecular diffusion only gets activated extremely close (tens of μm) to the crack tip. Both models predict exponential decay of crack-tip vapor concentration with increasing velocity (Fig. 10c).

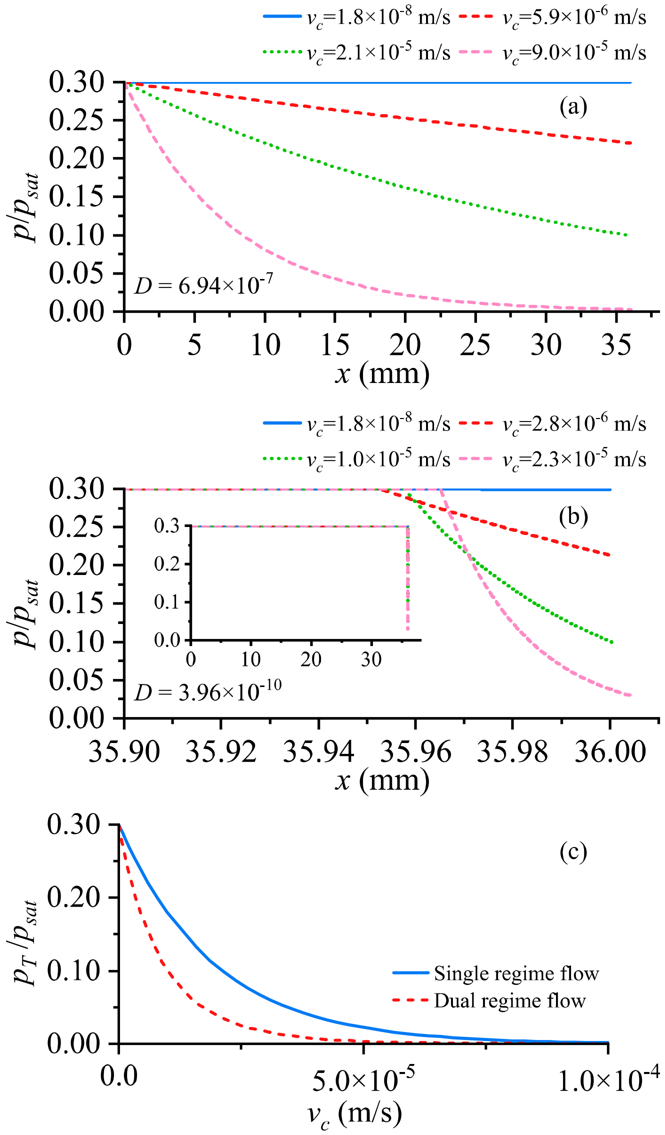

Fig. 10. Steady-state vapor partial pressure profile based on the (a) single-regime model Eq. (19), and (b) dual-regime model Eq. (20) at different crack velocities. (c) Crack-tip pressure exponentially decreases as crack velocity increases. The model parameters used are those of Table 3.

6. SOLUTION SCHEME

Our SFFT model specialized for glass SCG is now complete with fracture mechanics Eqns. (1) and (2), crack kinetics Eq. (7), surface force model Eqns. (9) and (10), and transport model Eq. (19) or (20). This section seeks the solution of the system subject to stress, $\sigma(t)$, over domain $x \in [0, a]$, and at each point in time t_k. Over each time increment $(t_k, t_k + \Delta t_k)$, the crack length is updated based on

$$a(t_k + \Delta t_k) = a(t_k) + v_c(t_k)\Delta t_k \tag{21}$$

where Δt_k is initially set to $0.05\,\text{sec}$. It is reduced if the relative error at t_k is small and increased if the relative error is large, within the range of $0.02\,\text{sec} - 1\,\text{sec}$.

For spatial discretization, nodes are distributed along the crack at the mid-plane, permitted by the one-dimensional nature of the problem. The crack is divided by N nodal points located at $(x_1, x_2, ..., x_N)$ that are densely distributed (~ every 6 nm) near the crack tip and coarsely distributed (~ every 70 μm) close to the crack mouth. This is because of the nature of surface forces: they take large magnitudes and vary dramatically at short separations, then diminish quickly as the separation increases, making the system extremely non-linear near the crack tip. With this discretization, the unknown vectors $\mathbf{p}$, $\mathbf{w}$, and $\mathbf{\Pi}$ are defined as $p_i = p(x_i)$, $w_i = w(x_i)$, and $\Pi_i = \Pi(x_i)$, respectively.

For the modularity of the numerical scheme, the equations are grouped in three subsystems: **S1**) the fluid transport subsystem, Eq. (19) or (20); **S2**) the fracture mechanics $\Pi - w$ subsystem, Eqns. (1), (2), (9), and (10); and **S3**) the crack propagation subsystem, Eq. (7). They are then iteratively coupled at the global level to search for a solution that simultaneously satisfies all the underlying equations.

For S1, the transport models in Eqns. (19) and (20) provide explicit solution at all points. In discrete form, the nodal pressure described by these models are, respectively,

$$p_i = p_0 \exp\left(-\frac{v_c}{D} x_i\right) \tag{22}$$

and

$$p_i = \begin{cases} p_0 & ; \quad \forall x_i \mid w(x_i) > w_{th} \\ p_0 \exp\left(-\frac{v_c}{D}(x_i - a + d)\right) & ; \quad \forall x_i \mid w(x_i) \leq w_{th} \end{cases} \tag{23}$$

x_i is the coordinate of node i in the coordinate system set at the crack mouth, consistent with that used for the fracture mechanics solution (Fig. 3). For S2, an iterative method is required to solve the $\Pi - w$ equations at fixed p profiles. Consistent Π and w profiles together with the resultant K_{Ie} are obtained by following the solution method of Planas and Elices (1991), while taking advantage of the analytical solutions made available by Tada et al. (2000) (Appendix A). For S3, Eq. (7) simply inputs an effective stress intensity and outputs the resultant crack velocity.

The global coupling of S1, S2, and S3 is achieved through a partitioned Newton-Raphson method. This method follows the multi-level Newton method of Kim et al. (2003). At local level, S1, S2, and S3 are solved separately and independently. It is important to distinguish the global unknowns as the guessed inputs and the response of each subsystem to its pertaining guessed inputs as the local outputs. The global unknowns are defined here as the partial pressure of the adsorptive fluid, $\mathbf{p}$; the crack opening, $\mathbf{w}$; the effective stress intensity factor at the crack tip, K_{Ie}; and the crack velocity, v_c. We shall then denote the solution to the fluid profile in response to guess values of crack opening and crack velocity by $\hat{\mathbf{p}}(\mathbf{w}, v_c)$, solved by S1; the crack opening and effective stress intensity in response to guess values of fluid state profile by $\hat{\mathbf{w}}(\mathbf{p})$ and $\hat{K}_{Ie}(\mathbf{p})$, solved by S2; and the crack propagation velocity in response to a guess value of stress intensity factor by $\hat{v}_c(K_{Ie})$, solved by S3. The coupling is achieved by directing the global residual to zero in an iterative manner.

The vector of global unknowns is constructed as

$$\mathbf{u} = \begin{bmatrix} \mathbf{p} \\ \mathbf{w} \\ K_{Ie} \\ v_c \end{bmatrix} \tag{24}$$

The global residual is defined as

$$\mathbf{R} = \begin{bmatrix} \mathbf{p} - \hat{\mathbf{p}}(\mathbf{w}, v_c) \\ \mathbf{w} - \hat{\mathbf{w}}(\mathbf{p}) \\ K_{Ie} - \hat{K}_{Ie}(\mathbf{p}) \\ v_c - \hat{v}_c(K_{Ie}) \end{bmatrix} \tag{25}$$

where $\mathbf{p}$, $\mathbf{w}$, K_{Ie}, and v_c are the values of the unknowns at the current iteration. The global solution that simultaneously satisfies S1, S2, and S3 can be found by iteratively marching towards $\mathbf{R} = \mathbf{0}$ via the Newton-Raphson method. In each iteration, the correction to $\mathbf{u}$, $\delta\mathbf{u}$, can be obtained from $\delta\mathbf{u} = -\mathbf{J}^{-1}(\mathbf{u}) \cdot \mathbf{R}(\mathbf{u})$ where $\mathbf{J}$ is the global Jacobian matrix defined as:

$$\mathbf{J} = \frac{\partial \mathbf{R}}{\partial \mathbf{u}} = \begin{bmatrix} \frac{\partial\left(\mathbf{p} - \hat{\mathbf{p}}(\mathbf{w}, v_c)\right)}{\partial \mathbf{p}} & \frac{\partial\left(\mathbf{p} - \hat{\mathbf{p}}(\mathbf{w}, v_c)\right)}{\partial \mathbf{w}} & \frac{\partial\left(\mathbf{p} - \hat{\mathbf{p}}(\mathbf{w}, v_c)\right)}{\partial K_{Ie}} & \frac{\partial\left(\mathbf{p} - \hat{\mathbf{p}}(\mathbf{w}, v_c)\right)}{\partial v_c} \\ \frac{\partial\left(\mathbf{w} - \hat{\mathbf{w}}(\mathbf{p})\right)}{\partial \mathbf{p}} & \frac{\partial\left(\mathbf{w} - \hat{\mathbf{w}}(\mathbf{p})\right)}{\partial \mathbf{w}} & \frac{\partial\left(\mathbf{w} - \hat{\mathbf{w}}(\mathbf{p})\right)}{\partial K_{Ie}} & \frac{\partial\left(\mathbf{w} - \hat{\mathbf{w}}(\mathbf{p})\right)}{\partial v_c} \\ \frac{\partial\left(K_{Ie} - \hat{K}_{Ie}(\mathbf{p})\right)}{\partial \mathbf{p}} & \frac{\partial\left(K_{Ie} - \hat{K}_{Ie}(\mathbf{p})\right)}{\partial \mathbf{w}} & \frac{\partial\left(K_{Ie} - \hat{K}_{Ie}(\mathbf{p})\right)}{\partial K_{Ie}} & \frac{\partial\left(K_{Ie} - \hat{K}_{Ie}(\mathbf{p})\right)}{\partial v_c} \\ \frac{\partial\left(v_c - \hat{v}_c(K_{Ie})\right)}{\partial \mathbf{p}} & \frac{\partial\left(v_c - \hat{v}_c(K_{Ie})\right)}{\partial \mathbf{w}} & \frac{\partial\left(v_c - \hat{v}_c(K_{Ie})\right)}{\partial K_{Ie}} & \frac{\partial\left(v_c - \hat{v}_c(K_{Ie})\right)}{\partial v_c} \end{bmatrix} \tag{26}$$

Upon simplification, one has

$$\mathbf{J}=\left[\begin{array}{c:c:c:c}\mathbf{I} & -\dfrac{\partial\hat{\mathbf{p}}}{\partial\mathbf{w}} & \mathbf{0} & -\dfrac{\partial\hat{\mathbf{p}}}{\partial v_c} \\ \hdashline -\dfrac{\partial\hat{\mathbf{w}}}{\partial\mathbf{p}} & \mathbf{I} & \mathbf{0} & \mathbf{0} \\ \hdashline -\dfrac{\partial\hat{K}_{Ie}}{\partial\mathbf{p}} & \mathbf{0} & 1 & 0 \\ \hdashline \mathbf{0} & \mathbf{0} & -\dfrac{\partial\hat{v}_c}{\partial K_{Ie}} & 1\end{array}\right] \tag{27}$$

A schematic of this partitioned Newton-Raphson scheme is presented in Fig. 11 for clarity.

The derivatives in Eq. (27) can be computed from Eq. (7), Eqns. (A.6) and (A.7) of Appendix A, and Eq. (22) or (23) depending on the choice of the transport model:

$$\frac{\partial\hat{v}_c}{\partial K_{Ie}}=\frac{v_0\kappa_0}{RT}\exp\left(-\frac{Q_0}{RT}\right)\cosh\left(\frac{\kappa_0 K_{Ie}}{RT}\right) \tag{28}$$

$$\frac{\partial\hat{w}_i}{\partial p_j}=c_{\Pi,ik}\frac{\partial\hat{\Pi}_k}{\partial p_j}\approx c_{\Pi,ik}\frac{\partial\Pi_k}{\partial p_j} \tag{29}$$

$$\frac{\partial\hat{K}_{Ie}}{\partial p_j}=k_{I\Pi,k}\frac{\partial\hat{\Pi}_k}{\partial p_j}\approx k_{I\Pi,k}\frac{\partial\Pi_k}{\partial p_j} \tag{30}$$

$$\frac{\partial\hat{p}_i}{\partial w_j}=\frac{\partial\hat{p}_i}{\partial d}\frac{\partial d}{\partial w_j}\approx 0 \tag{31}$$

$$\frac{\partial\hat{p}_i}{\partial v_c}=-\frac{x_i}{D}p_0\exp\left(-\frac{v_c}{D}x_i\right) \tag{32}$$

for single-regime flow, and

$$\frac{\partial \hat{p}_i}{\partial v_c} = \begin{cases} 0 & ; \quad \forall x \,|\, w(x) > w_{th} \\ -\dfrac{x_i - a + d}{D} p_0 \exp\left(-\dfrac{v_c}{D}(x_i - a + d)\right) & ; \quad \forall x \,|\, w(x) \le w_{th} \end{cases} \tag{33}$$

for dual-regime flow.

The errors are defined as

$$\varepsilon_p = \left|\frac{\delta p_i}{p_i}\right|, \ \varepsilon_w = \left|\frac{\delta w_i}{w_i}\right|, \ \varepsilon_{K_{Ie}} = \left|\frac{\delta K_{Ie}}{K_{Ie}}\right|, \text{ and } \varepsilon_{v_c} = \left|\frac{\delta v_c}{v_c}\right| \tag{34}$$

The iterations continue until the maximum of the four errors falls within a tolerance of 10^{-5}.

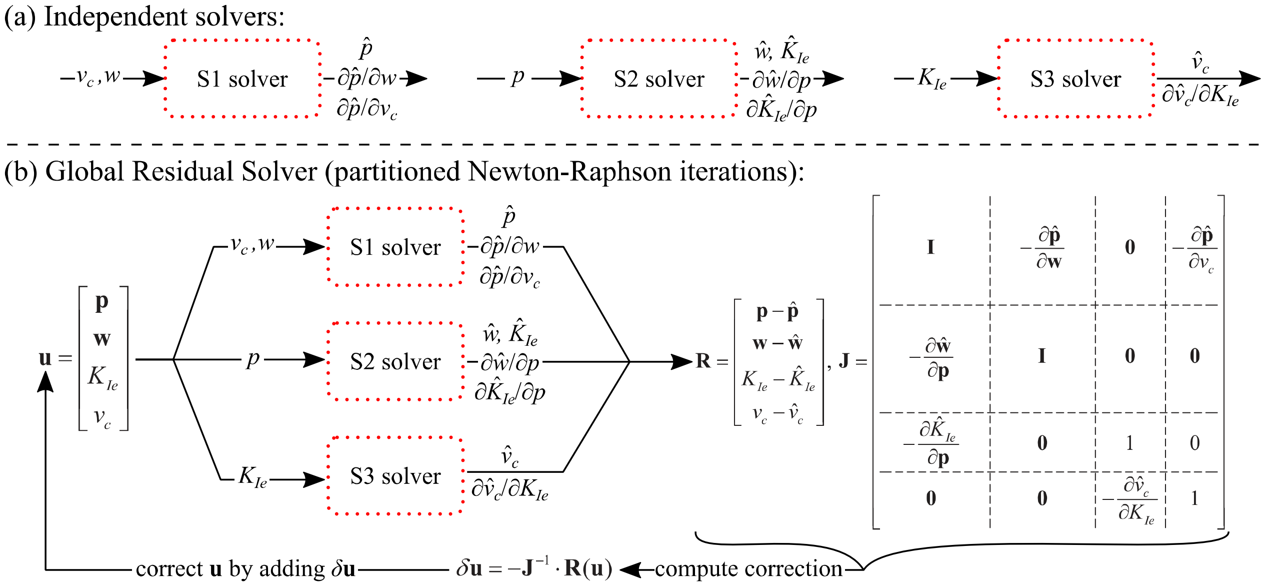

Fig. 11. A schematic of (a) the inputs and outputs of the S1, S2, and S3 solvers; and (b) the partitioned Newton-Raphson scheme to seek solutions satisfying all subsystems.

Note that the length of the slow transport regime d varies continuously as the crack opens or closes, while the numerical representation of the crack opening $\mathbf{w}$ is discrete and does not allow smooth variation of d. Therefore, a linear interpolation for the value of $w(x)$ between two nodes is adopted to allow smooth variation of d. Consequently, the derivative $\partial d / \partial \mathbf{w}$ cannot be effectively computed without explicit expression of d. This term is expected to be small anyway given the initial guess for $\mathbf{w}$

is close to the solution. The derivative in Eq. (31) is thus approximated by zero. In addition, the $\partial\hat{\mathbf{\Pi}}/\partial\mathbf{p}$ term in Eq. (29) must be approximated since the $\Pi - w$ system is implicitly solved without being written in terms of $\mathbf{p}$. Two versions of the implementation were tested, one with $\partial\hat{\mathbf{\Pi}}/\partial\mathbf{p} \approx (\partial\hat{\mathbf{\Pi}}/\partial\mathbf{p})_{\hat{\mathbf{w}}}$ and $\partial\hat{\mathbf{w}}/\partial\mathbf{p}$ given by Eq. (29), and the other with $\partial\hat{\mathbf{w}}/\partial\mathbf{p} \approx \mathbf{0}$. The second approximation yielded better convergence and was adopted in the final implementation. Finally, a proper initial guess is required to start the search for the solution at each time t_{k+1} due to the highly nonlinear nature of the problem. A robust initial guess algorithm is described in Appendix B.

7. PERFORMANCE OF THE FRAMEWORK

This section compares the SFFT prediction against Wiederhorn's SCG data (Fig. 12) to validate the underlying hypotheses depicted in Fig. 1.

7.1. Model calibration

We shall calibrate the least coupled parts of the model first. The intrinsic material properties including the elastic parameters, in-vacuum surface force, and the reaction kinetic parameters are therefore calibrated first here. These parameters are expected to control the in-vacuum stage-III SCG response.

The standard Young's modulus of soda-lime glass is 70 GPa (572-1, 2012) while the reported ones in literatures vary between 50 GPa and 85 GPa (Meyland et al., 2021). A Poisson ratio in the range of $0.2 \sim 0.3$ has been reported in some studies (Li and Wei, 2020; Meyland et al., 2021; Xu et al., 2017). Within this ballpark, the selected elastic parameters are shown in Table 1.

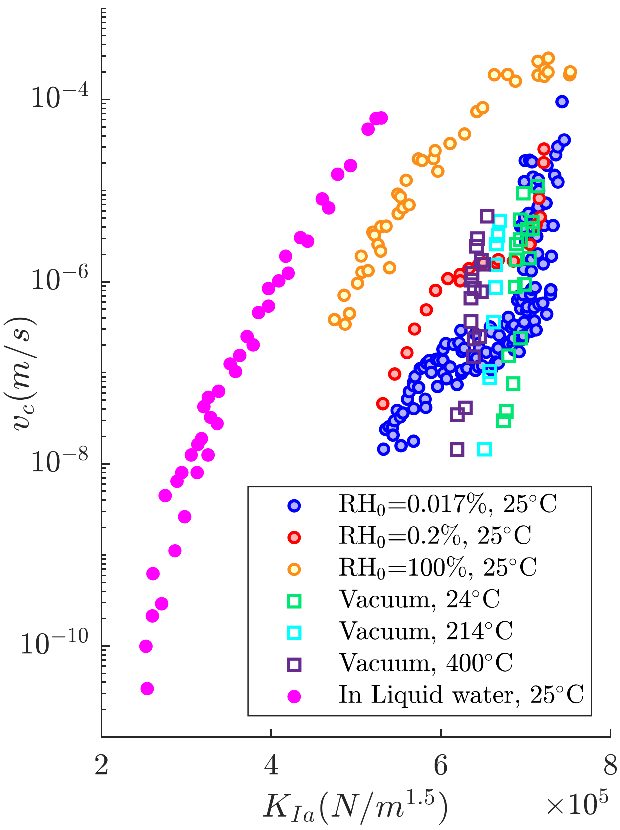

Fig. 12. Data for crack propagation in soda-lime glass at 25°C and different relative humidity (Wiederhorn, 1967; Wiederhorn et al., 1980), open circles; at different temperatures at 24°C, 214°C, and 400°C in vacuum (Wiederhorn, 1974), squares; and in liquid water (Wiederhorn and Bolz, 1970), filled circles.

Two types of data are adopted to calibrate the Π_0 parameters. The first data is surface energy for soda-lime glass measured by Wiederhorn (1969) at near room temperature in an environment with background nitrogen gas (inert) as $\gamma = 3.82\,\mathrm{J/m^2}$. This measurement in inert gas can estimate the area underneath the $\Pi_0 - w$ curve, in absence of sorptive species (Gdoutos, 2020). For the selected Π_0 expression Eq. (9), this area is $\gamma = \Pi_{0,\max} w_0$. The second data is the SFA measurements between a glass sphere in air (Yaminsky and Stewart, 2003), scaled by a factor of 912.6 such that the area underneath this data matches the surface energy measurement. Parameters $\Pi_{0,\max}$ and w_0 are then selected (Table 1) to match this data (Fig. 13).

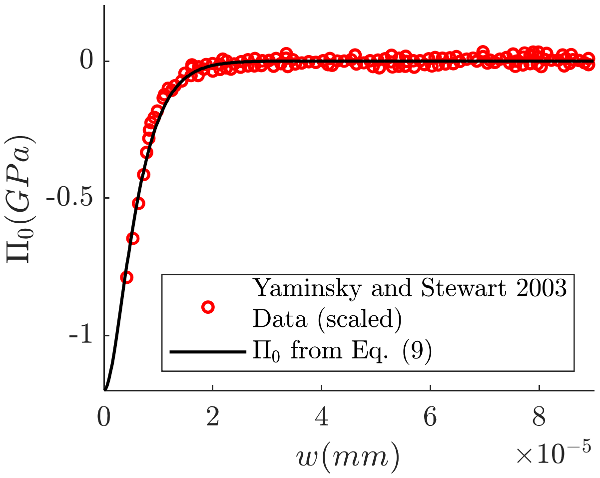

Fig. 13. Calibrated in-vacuum surface force ($\Pi_{0,\max}=1200\text{MPa}$ and $w_0=3.1833\times10^{-6}\text{mm}$) vs. SFA measurements. A constant multiplying factor is applied to the SFA data to roughly match the area under this curve with the surface energy measurement of $\gamma=3.82\text{J/m}^2$. The Π_0 data is converted from F/R data multiplied by 912.6.

The reaction kinetic parameters are calibrated against the in-vacuum v_c-K_{Ia} data. At relatively large K_{Ia} values, the $K_{Ie}-K_{Ia}$ relation becomes linear (see Fig. 6) and so does the $\log(v_c)-K_{Ie}$ relation (Eq. (7)). Combining the two gives a linear one-to-one correspondence between K_{Ia} and v_c at high K_{Ia} levels. Note that there are infinite combinations of v_0, Q_0, and κ_0 to match a linear set of $\log(v_c)-K_{Ia}$ data. Such arbitrariness can be removed by considering the temperature dependence of the crack kinetics. Specifically, the same set of v_0, Q_0, and κ_0 should capture the in-vacuum v_c-K_{Ia} curves obtained at different temperatures, assuming the Arrhenius term in Eq. (7) outweighs the temperature dependence of the elastic parameters and in-vacuum surface forces. Fig. 14 plots soda-lime glass v_c-K_{Ia} data obtained at 24°C, 214°C, and 400°C (Wiederhorn, 1974) based on which the kinetic parameters v_0, Q_0, and κ_0 are calibrated (Table 1). Their values are the same orders of magnitude as those presented in Wiederhorn (1974).

Table 1. Model parameters that control stage III SCG behavior

Parameter	Unit	Values
Elasticity		
E	[MPa]	50000
ν	[-]	0.2
In-vacuum surface force		
w_0	[mm]	3.1833×10^{-6}
$\Pi_{0,\max}$	[MPa]	1200
Crack propagation reaction		
v_0	[mm/s]	3.303×10^{5}
Q_0	[J/mol]	1.31×10^{5}
κ_0	[m$^{2.5}$/mol]	0.24

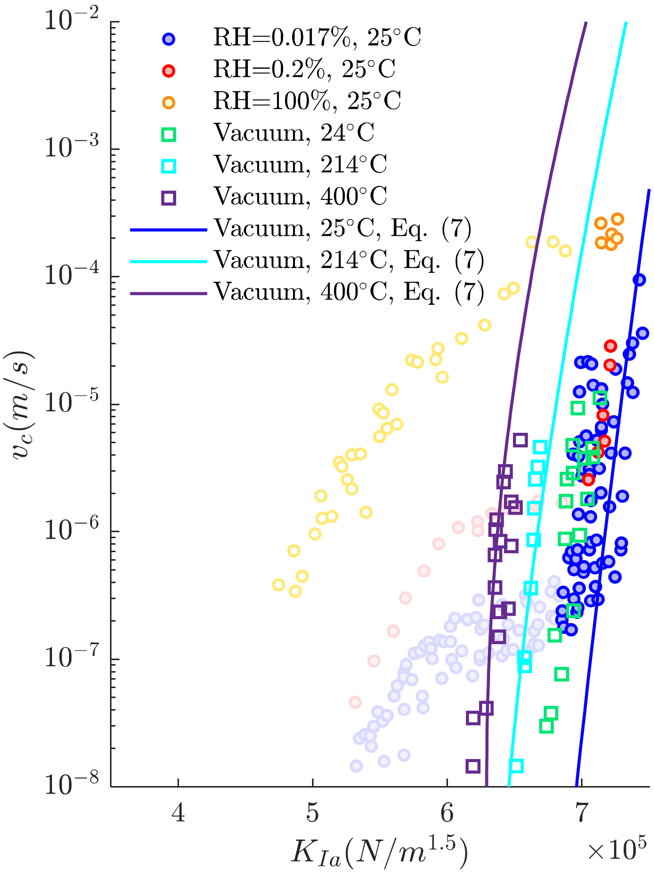

Fig. 14. Calibration of reaction rate parameters v_0, Q_0, and κ_0 against SCG data at three temperatures, 25°C, 214°C, and 400°C in vacuum. The irrelevant data are faded for clarity.

The model is now fully calibrated for the in-vacuum condition. We now move on to determine parameters that control the environmental dependency, specifically the environment-induced disjoining pressure $\Delta\Pi$ and the pressure profile $p(x)$. The former is expected to affect the strength reduction in stage I, and the latter limits the rate of crack propagation in stage-II SCG.

In Eqns. (10), (11), and (12), parameters $\Delta\Pi_{\max}$ and $\tilde{w}_0$ control the dependence of $\Delta\Pi$ on the crack opening and parameters α and β independently control the dependence of $\Delta\Pi$ on the partial pressure of the adsorbate. AFM measurements in glass-liquid water system (Acuña and Toledo, 2008) provides a benchmark for the shape of the $\Delta\Pi - w$ relation at $p = p_{sat}$ which allows the determination of $\tilde{w}_0$ (Fig. 15). The area underneath $\Delta\Pi$ reflects the change of surface energy in presence of water vapor, meaning that $\Delta\Pi_{\max}$ can be calibrated based on the reduction of apparent fracture toughness from $\mathrm{RH}_0 = 0\%$ to 100% (Fig. 16). Finally, parameters α and β in Eq. (12) are tuned to capture the strength reductions at $\mathrm{RH}_0 = 0.017\%$, 0.2%, 1%, 10%, and 30% (Fig. 16). These parameters are summarized in Table 2.

Table 2. Parameters that control stage I SCG in complement to Table 1.

Parameter	Unit	Values
Environment-induced disjoining pressure		
$\tilde{w}_0$	[mm]	1.8×10^{-5}
$\Delta\Pi_{0,\max}$	[MPa]	167
α	[-]	0.067
β	[-]	10^{-5}

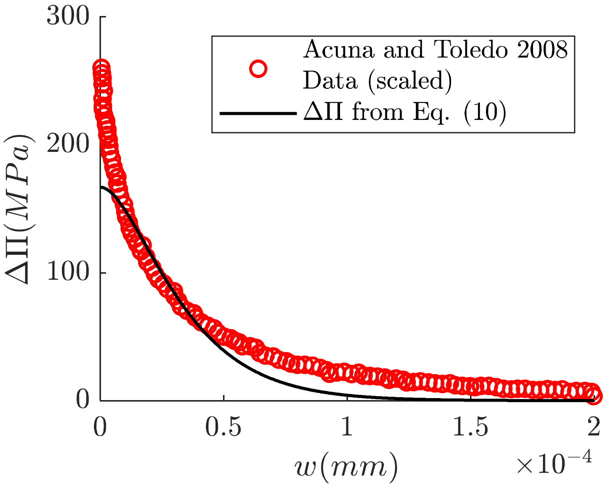

Fig. 15. Calibrated $\Delta\Pi$ with parameters $\tilde{w}_0 = 1.8\times10^{-5}$ mm and $\Delta\Pi_{\max} = 167\text{MPa}$ at $p = p_{sat}$ based on the *F*/*R* measurements from AFM (Acuña and Toledo, 2008) scaled by 120.5. The main purpose here is to match the shape via adjusting $\tilde{w}_0$. $\Delta\Pi_{\max}$ is determined in Fig. 16.

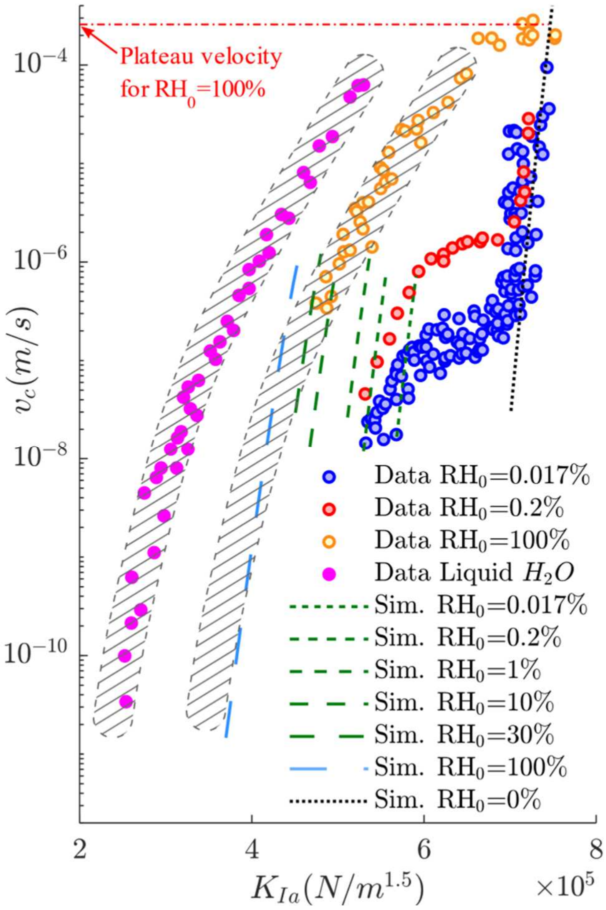

Fig. 16. Measured vs. simulated strength reduction at $\text{RH}_0 = 100\%$ with parameters $\Delta\Pi_{\max} = 167\text{MPa}$ and $\tilde{w}_0 = 1.8\times10^{-5}$ mm (light blue coarse-dashed line). The strength reductions for intermediate RH values are captured by selecting $\alpha = 0.067$ and $\beta = 10^{-5}$ (green dashed lines). The cross-hatching is meant as a visual guide for the extension of the

$\mathrm{RH}_0 = 100\%$ data based on the data in liquid water. The reason for this extension is to obtain a visual of the $\mathrm{RH}_0 = 100\%$ curve at lower velocities for the purpose of calibration.

On the transport side, for both $p(x)$ profiles depicted by Eq. (19) and Eq. (20) , D is selected such that the adsorbate relative pressure at the crack tip drops to an arbitrary small value (here taken as 2×10^{-6}) at the stage-II plateau velocity for the $\mathrm{RH}_0 = 100\%$ case ($v_c = 2.5\times10^{-4}\,\mathrm{m/s}$ at $K_{Ia} = 7.44\times10^5\,\mathrm{N/m}^{1.5}$ from Fig. 16). The near-tip region length d for the dual-regime flow model is estimated from the in-vacuum crack opening profile at $K_{Ia} = 7.44\times10^5\,\mathrm{N/m}^{1.5}$. This gives $d \approx 2.13\times10^{-5}\,\mathrm{m}$; i.e., $w < w_{th} = \lambda / \mathrm{Kn}_0$ for $a - 2.13\times10^{-5} < x$. The values of D for the two cases are given in Table 3.

Table 3. Parameters that control stage II SCG in complement to Table 1 and Table 2.

Parameter	Unit	Values
Single-regime flow		
D	$[\mathrm{m}^2/\mathrm{s}]$	6.94×10^{-7}
Dual-regime flow		
D	$[\mathrm{m}^2/\mathrm{s}]$	3.96×10^{-10}

These calibrated D values can be quantitatively compared with some theoretical estimates. In a study of gas transport in shale nanopores, Wu et al. (2015) predicted an equivalent Darcian permeability k (as in $v_{fluid} = -(k/\mu)\partial p/\partial x$) of order $10^{-17}\,\mathrm{m}^2$ for the case of surface diffusion. Conversion of k to D can be made by rewriting $J(x) = -D\partial n/\partial x$ as $v_{fluid} = J/n = -(D/p)\partial p/\partial x$, giving $D = kp/\mu$. A viscosity of order $10^{-5}\,\mathrm{Pa\cdot s}$ is assumed (Tsilingiris, 2008; Wu et al., 2015), and a pressure of order $< 10^3\,\mathrm{Pa}$ can be assumed considering $O(p_{sat}) = 10^3\,\mathrm{Pa}$ for water vapor. This gives . $O(D_{\text{surf. diff.}}) < 10^{-9}\,\mathrm{m}^2/\mathrm{s}$. for surface diffusion, comparable with the calibrated value of D for dual-regime flow. Similar comparison can be made in the case of Knudsen diffusion (Wu et al., 2015). On the other hand, considering viscous flow in a slit with aperture w, one can derive $D_{\text{bulk flow}} = RTw^2 / 12\mu V_m$ for ideal gas. At room temperature, the molar volume of ideal gas is $V_m = 2.45\times10^{-2}\ \text{m}^3/\text{mol}$. Fig. 5 suggests that the crack opening varies from order $10^{-5}\,\text{m}$ to $10^{-8}\,\text{m}$ from the crack mouth to where surface forces are observed. Combining the above gives $O(D_{\text{bulk flow}}) = 10^{-2} \sim 10^{-8}\,\text{m}^2/\text{s}$. Note that the estimated $D_{\text{bulk flow}}$ is several orders larger than our calibrated D values (Table 3) and those estimated based on Wu et al. (2015). This justifies our assumption that the pressure drop is negligible in the bulk flow regime up to the transition point (Fig. 9c).

7.2. Model prediction

Using the calibrated parameters in Tables 1, 2, and 3, the SCG curves predicted by the SFFT model for single-regime and dual-regime flow at $\text{RH}_0 = 100\%$ are presented together with experimental data in Fig. 17a. It is exciting to see that, for the first time, the key features of all three stages of SCG and the smooth transition between them are directly predicted by a single mechanistic model. Comparing the two computed SCG curves suggests that the choice of transport model directly impacts the stages I and II SCG behavior. This cannot be observed in existing phenomenological SCG models, since the shape of the whole SCG curve is imposed rather than predicted in these approaches (Charles, 1962; Lawn, 1975). Fig. 17b presents the predicted vapor pressure profiles at different stages of SCG for the dual-regime model. As K_{Ia} increases, the crack opening widens, and the inviscid regime moves closer to the crack tip. However, the simultaneous increase in crack velocity outpaces the crack widening, which results in an overall decrease of fluid concentration at the crack tip. Fig. 17c shows that the disjoining pressure is extremely concentrated near the crack tip and is highly sensitive to the local vapor pressure and thus the crack velocity. This suggests that the introduction of slight repulsive disjoining pressure in the near-tip region can cause significant reduction of the apparent fracture toughness for brittle solids. The profiles plotted in Fig. 17b and c confirm the common speculation that fluid transport is indeed the rate-limiting mechanism for the stage II of SCG.

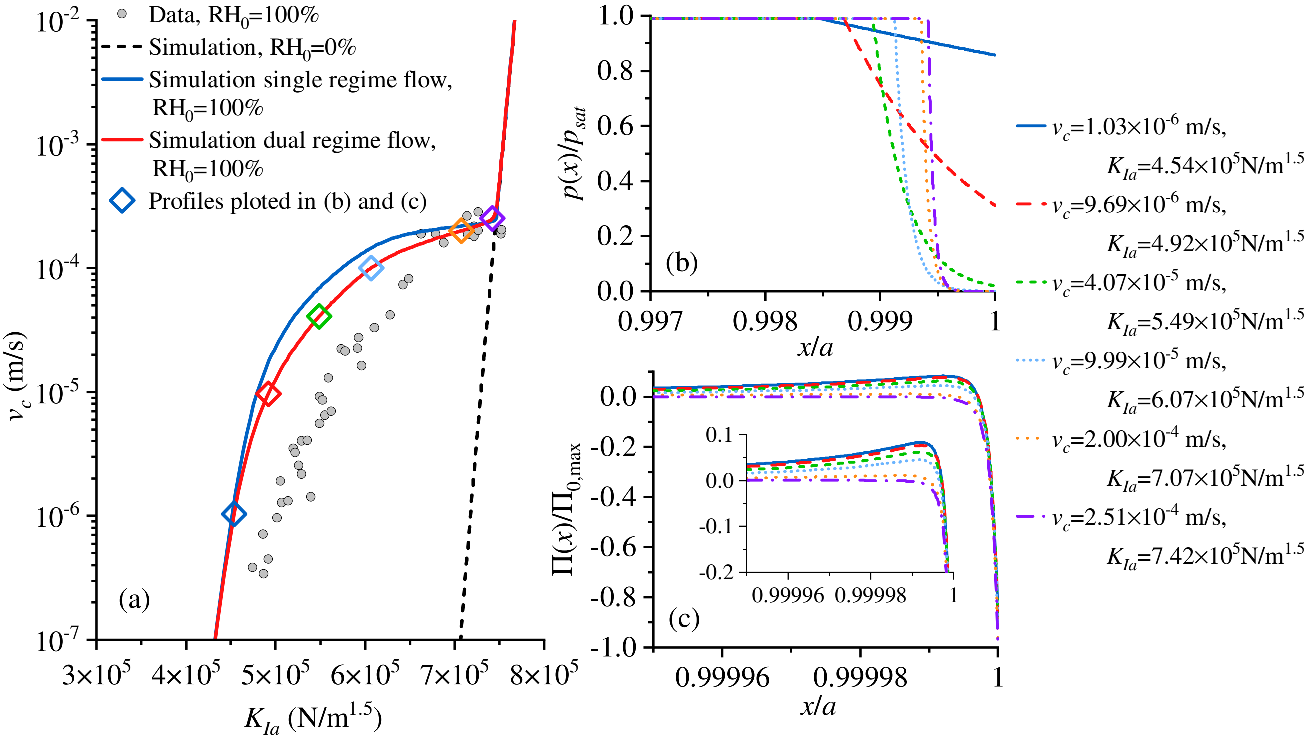

Fig. 17. (a) Measured vs. predicted SCG curves at RH_0 =100% based on single-regime flow and dual-regime flow. (b) Pressure profiles at different stages along the SCG curve depicted by the dual-regime flow model. (c) Disjoining pressure distribution at different stages along the SCG curve.

Recalling that the SFFT model was calibrated only for the apparent toughness (where the SCG curve intersects with the $x-$axis) and the plateau velocity (where stages II and III intersects) at $\mathrm{RH}_0 = 100\%$, everything in between should be regarded as true predictions. It is observed that the current model generally overestimates the crack velocity in stages I and II, with the dual regime flow model making slightly better prediction. This is because the experimental data suggests the stage-I slope is lower compared to the in-vacuum portion, while the current model predicts the same slopes for stages I and III. We may remediate this through the reaction rate parameters or the fluid transport parameters. Fig. 18a demonstrates that the decrease of κ_0 or Q_0 can reduce the slope of SCG curve in the $\log(v_c)-K_{Ia}$ plane. This implies that the lowered stage-I slope can be accounted for by introducing some environmental dependency on the kinetic parameters. A rigorous proposal of $\kappa_0(p)$ or $Q_0(p)$ requires detailed study of how the energy barrier for bond rupture at the very crack tip lowers under environmental attack, which is beyond the scope of this paper. Alternatively, an apparent slope reduction can be readily observed by cropping out the very low velocity range of the SCG plots (Fig. 18b).

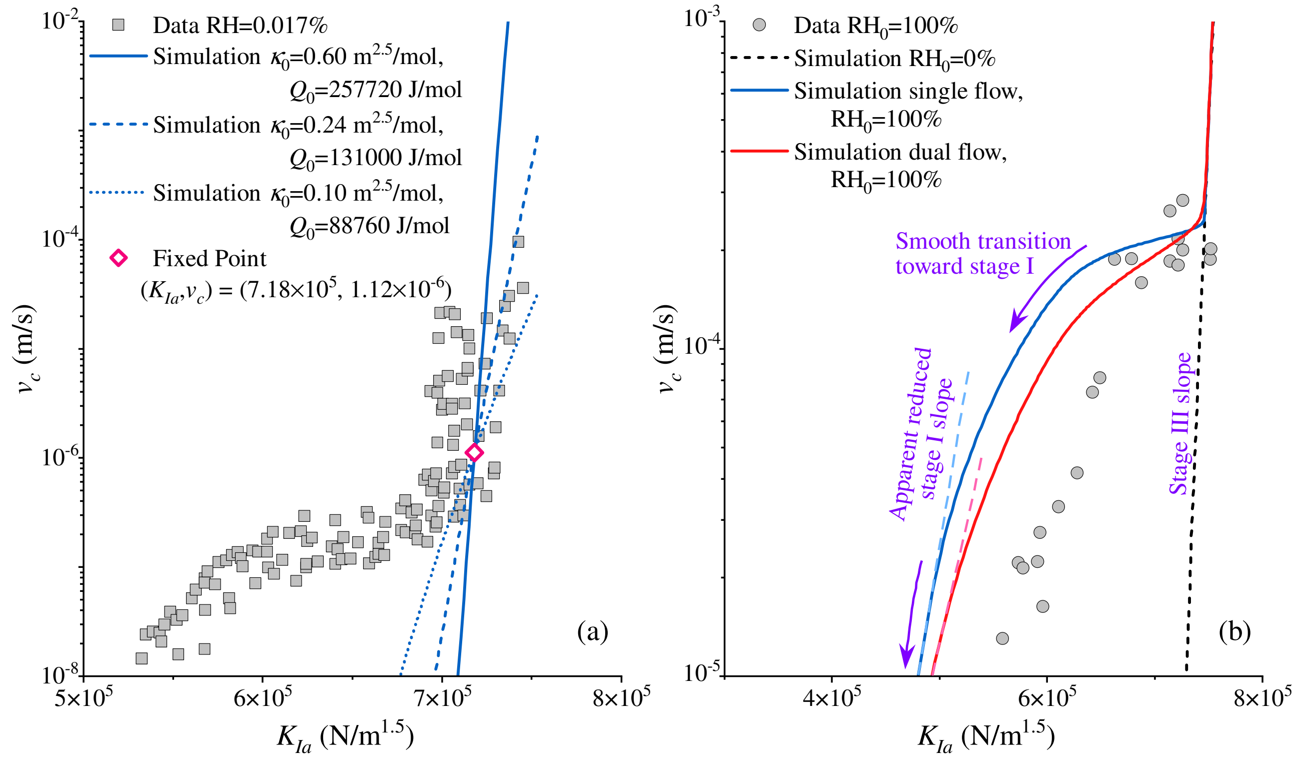

Fig. 18. (a) Variation of SCG slope about a fixed point ($K_{Ia} = 7.18\times10^5\,\text{N/m}^{1.5}$ and $v_c = 1.12\times10^{-6}\,\text{m/s}$) controlled by parameters κ_0 and Q_0 : $\kappa_0 = 0.60\,\text{m}^{2.5}/\text{mol}$ and $Q_0 = 257720\,\text{J/mol}$ for Simulation A; $\kappa_0 = 0.24\,\text{m}^{2.5}/\text{mol}$ and $Q_0 = 131000\,\text{J/mol}$ for Simulation B; and $\kappa_0 = 0.10\,\text{m}^{2.5}/\text{mol}$ and $Q_0 = 88760\,\text{J/mol}$ for Simulation C. (b) Zoomed-in presentation of Fig. 17 giving an impression of reduced stage-I slope.

This implies that a rate-limiting mechanism that is activated over a wide range of crack velocities can cause the reduced slope in stage I. Perhaps a mechanism with weaker dependence on v_c compared to the current transport models (e.g., a different near-tip diffusion mechanism, or sorption kinetics) can potentially close this gap. In partial support of this hypothesis, the experimental SCG data for crack propagation in liquid water in Fig. 16 which extends to much lower crack propagation velocities shows a slope close to the in-vacuum one. This speculation challenges the commonly accepted picture that SCG in stage I is free from any rate-limiting influences. More investigations are required in this regard to clarify the origin of environment-dependent slope in stage I SCG.

Fig. 19 presents the predicted SCG curves over a range of relative humidity from 0% to 100%.

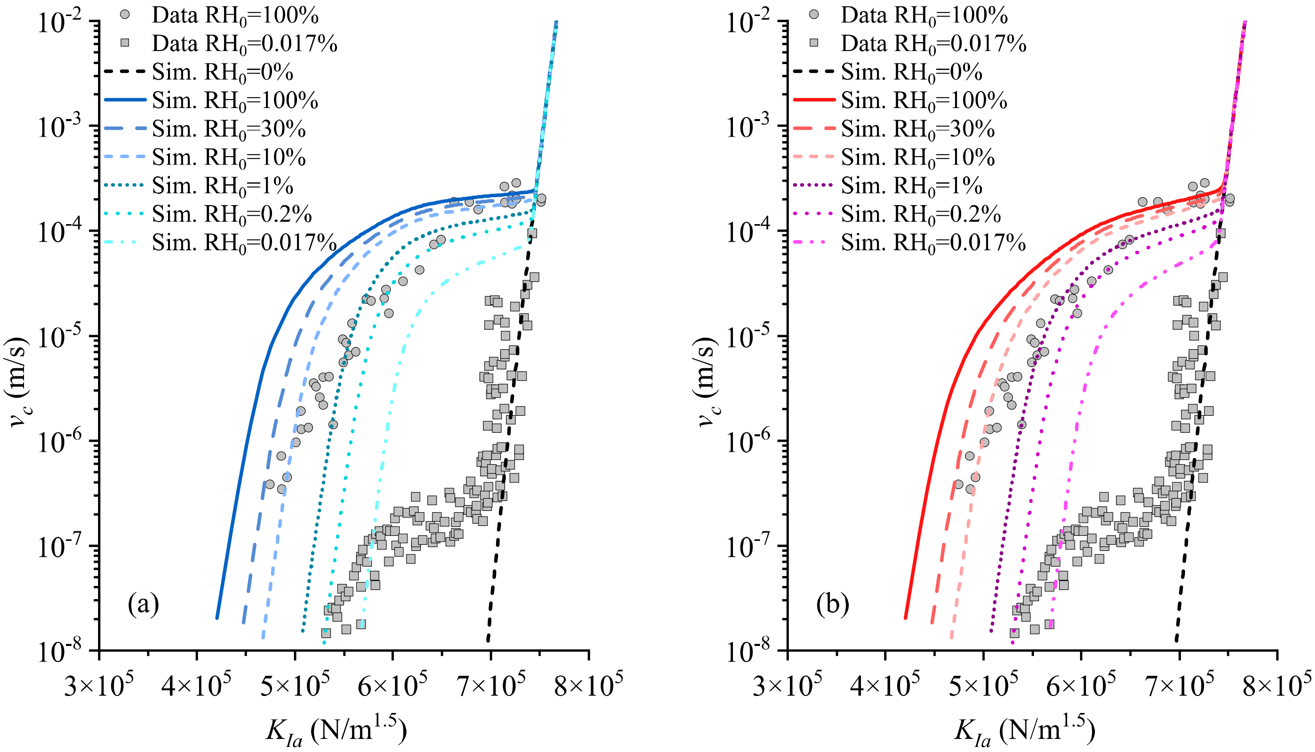

Fig. 19. Measured vs. predicted SCG curves at different RH$_0$ values based on (a) single regime flow and (b) dual regime flow models.

It is observed that both flow models significantly underestimate the variation of plateau velocities at different humidity levels. Based on our previous observation that the shape of SCG critically depends on the transport model, we suspect that this underprediction is related to the insensitivity of the vapor pressure profile $p(x)$ to the RH_0. Physically, the threshold crack width w_{th} characterizing the point of transition from bulk flow to molecular diffusion (point C in Fig. 9c) should not be a constant but rather vary with respect to the boundary conditions (i.e., the ambient humidity). This possibility is explored in the next subsection.

7.3. Effect of variable w_{th}

Intuitively, lower RH means less water molecules in the environment, and they can be more easily captured by the crack walls to form the first few adsorbed layers. This promotes the molecular diffusion of water in adsorbed states rather than free bulk gas flow, thus extending the length of the "boundary layer" d in Fig. 9a. w_{th} is therefore proposed to be inverse proportional to RH_0. A simple proposition to account for this effect is:

$$w_{th} = \frac{\lambda / \mathrm{Kn}_0}{1 + h_0(\mathrm{RH}_0 - 1)} \tag{35}$$

where $h_0 < 1$ is a parameter to control how rapid w_{th} varies with RH_0 such that $w_{th}(\mathrm{RH}_0 = 1) = \lambda / \mathrm{Kn}_0$. Here, a value of $h_0 = 0.919$ is found to match the plateau velocity for case of $\mathrm{RH}_0 = 0.017\%$. The predicted SCG curves using the updated w_{th}, Eq. (35), for all other RH_0 values are presented in Fig. 20. We can see that the SFFT model is now capable of quantitatively capturing the shifting of the plateau velocity and the apparent fracture toughness under humidity changes. Again, this observation highlights the importance of detailing the transport of sorptive species in the near-tip regime in order to correctly predict the SCG behavior of brittle solids under various ambient conditions.

A subcritical cracking "stage diagram" can be produced (Fig. 21) in the normalized $\log(v_c / v_0) - (K_{Ia} / \sqrt{2E'\gamma})$ space based on the slope of the predicted SCG curves in Fig. 20. The slope in the normalized space is defined as $I_c = d\log(v_c / v_0) / d(K_{Ia} / \sqrt{2E'\gamma})$, which is analogous to the *corrosion index* in the Charles' law (Atkinson, 1982).

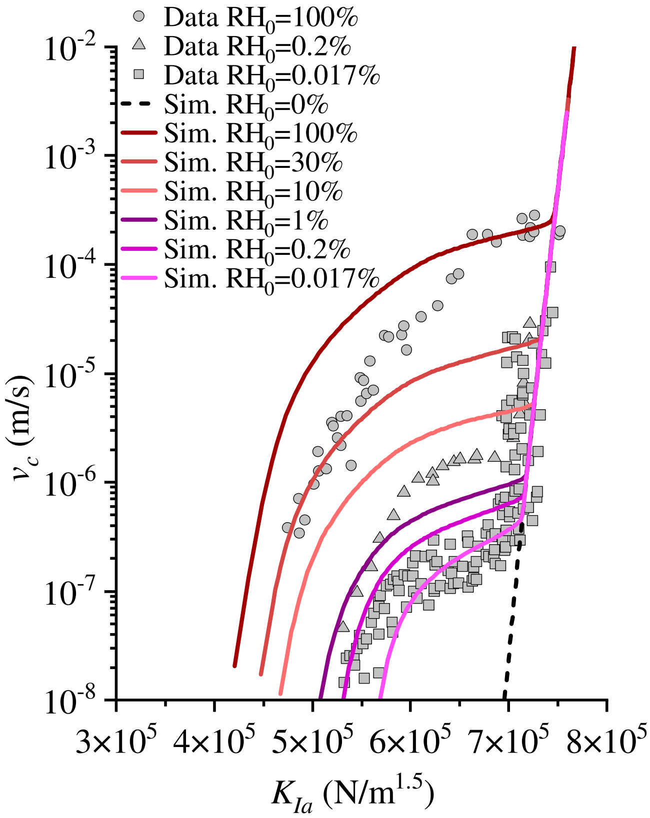

Fig. 20. Measured vs. predicted SCG curves at different RH$_0$ values based on dual-regime flow and RH$_0$-dependent w_{th} (Eq. (35) with $h_0 = 0.919$).

It is apparent in Fig. 21 that stages I and III are represented by regions with larger I_c, while a drop of I_c to lower values indicates stage II. Transition from stage II to III occurs abruptly (cyan dash-dot line), while the transition from stage I to II happens gradually with a much smoother and wider variation of I_c values in between. A value of $I_c = 15$ is selected to roughly represent this transition (pink dashed line). Fig. 21 predicts that increased ambient relative humidity expands the stage-II zone, indicating that species transport becomes more dominating in shaping the SCG curve over a wider K_{Ia} range at high RH levels. If an SCG curve is plotted in a limited range of K_{Ia} and thus v_c, one would have concluded that the apparent corrosion index (i.e., the slope) is reduced as a function of the ambient humidity. This reiterates one of our earlier speculations that the reduced slopes in stage I SCG could be just a visual impression of an extended stage II zone due to the slow transport of environmental agents.

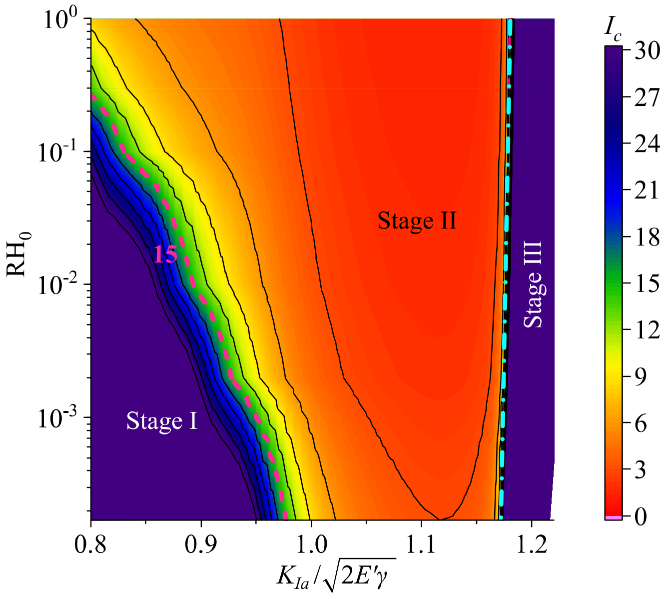

Fig. 21. A dimensionless stage diagram for SCG. Color indicates the slopes of normalized v_c / v_0 versus $K_{Ia} / \sqrt{2E'\gamma}$ curves from Fig. 20, based on which the three SCG stages can be clearly identified.

8. CONCLUSION

This study develops a surface-force based fracture theory (SFFT) to rationalize and predict the subcritical cracking of brittle solids in sorptive environments. The theory highlights the fundamental role of surface forces which present at a few tens of nanometer surface-surface separations on the apparent fracture toughness, its environmental dependency, and the crack growth kinetics of SCG. Specifically, analytical LEFM solutions are adopted to consider the repulsive disjoining force induced by sorption behind the crack tip. The competition between the material's intrinsic cohesive forces and environment-induced disjoining forces is manifested as the *effective stress intensity factor* operating at the crack tip and serves as the driving force for crack propagation. This quantitatively explains the environmentally induced strength reduction of brittle solids. The characteristic shape of the SCG curve is further impacted by the rate-limiting effect of species transport in the crack. Simplified analytical transport models are proposed to qualitatively represent the single-regime and dual-regime flows. Finally, the model is validated against the experimental data on soda-lime glass in water vapor studied by Wiederhorn (1967). The main findings of this study are highlighted below:

1. The development of repulsive disjoining pressure behind the crack tip in sorptive environment can cause the reduction of apparent fracture toughness.
2. Species transport along the crack is the rate-controlling mechanism governing the plateau velocity and the stage-II behavior of SCG.
3. The effect of transport can go beyond stage II and shape the characteristics of stage-I SCG curve, for example, by reducing the apparent slope in stage I.
4. The SCG stage diagram generated by SFFT simulations allows one to visualize the conditions for each stage of SCG and the characteristics of transition between stages.

The theory and its numerical solution scheme are set up in such a way that more complex and advanced model components can be readily incorporated for extensions to other brittle materials. Further improvements can be contemplated by (1) incorporating more realistic fluid transport models that automatically capture the smooth transition between different transport mechanisms as the crack aperture varies; (2) considering the underlying sources of surface forces to motivate a physics-based disjoining pressure model; and (3) extending to different systems such as the SCG of quartz or calcite in aqueous solutions for geoscience and geo-engineering applications. Some fundamental aspects require further investigations to enrich the calibration and validation of SFFT. For example, experimental studies and molecular dynamic simulations are needed to quantify disjoining pressure between freshly exposed solid surfaces in sorptive environment and to better understand species transport in nano-confined spaces.

ACKNOWLEDGEMENT

This research was supported by the U.S. Department of Energy, Office of Science, Office of Basic Energy Sciences, Chemical Sciences, Geosciences, and Biosciences Division, through its Geoscience program at LBNL under Contract DE-AC02-05CH11231 and through Subcontract NO. 7556334 to the University of Colorado Boulder.

REFERENCES

572-1, D.E., 2012. Glass in Building–Basic Soda Lime Silicate Glass Products–Part 1: Definitions and General Physical and Mechanical Properties. Beuth Verlag Berlin.

Acuña, S.M., Toledo, P.G., 2008. Short-range forces between glass surfaces in aqueous solutions. Langmuir 24, 4881-4887.

Adapa, S., Malani, A., 2021. Role of cation size on swelling pressure and free energy of mica pores. Journal of Colloid and Interface Science 599, 694-705.

Adler, J.J., Rabinovich, Y.I., Moudgil, B.M., 2001. Origins of the non-DLVO force between glass surfaces in aqueous solution. Journal of colloid and interface science 237, 249-258.

Allegri, G., 2020. A unified formulation for fatigue crack onset and growth via cohesive zone modelling. Journal of the Mechanics and Physics of Solids 138, 103900.

Ash, S.G., Everett, D.H., Radke, C., 1973. Thermodynamics of the effects of adsorption on interparticle forces. Journal of the Chemical Society, Faraday Transactions 2 69, 1256.

Atkinson, B.K., 1982. Subcritical crack propagation in rocks: theory, experimental results and applications. Journal of Structural Geology 4, 41-56.

Atkinson, B.K., 1984. Subcritical crack growth in geological materials. Journal of Geophysical Research: Solid Earth 89, 4077-4114.

Barenblatt, G.I., 1962. The mathematical theory of equilibrium cracks in brittle fracture. Advances in applied mechanics 7, 55-129.

Bažant, Z.P., Oh, B.H., 1983. Crack band theory for fracture of concrete. Matériaux et construction 16, 155-177.

Bazant, Z.P., Planas, J., 1997. Fracture and size effect in concrete and other quasibrittle materials. CRC press.

Bird, R.B., Stewart, W.E., Lightfoot, E.N., 2006. Transport phenomena. John Wiley & Sons.

Brantut, N., Heap, M., Meredith, P., Baud, P., 2013. Time-dependent cracking and brittle creep in crustal rocks: A review. Journal of Structural Geology 52, 17-43.

Brunauer, S., Deming, L.S., Deming, W.E., Teller, E., 1940. On a Theory of the van der Waals Adsorption of Gases. Journal of the American Chemical Society 62, 1723–1732.

Chapman, S., Cowling, T.G., 1990. The mathematical theory of non-uniform gases: an account of the kinetic theory of viscosity, thermal conduction and diffusion in gases. Cambridge university press.

Charles, R., 1958. Static fatigue of glass. I. Journal of Applied Physics 29, 1549-1553.

Charles, R., 1962. The kinetics of glass failure by stress corrosion. Simposium sur la Resistance Mechanique du Verre et les Moyens de l'Ameliorer 511.

Chester, F., Chester, J., Kronenberg, A., Hajash, A., 2007. Subcritical creep compaction of quartz sand at diagenetic conditions: Effects of water and grain size. Journal of Geophysical Research: Solid Earth 112.

Choi, J.-G., Do, D., Do, H., 2001. Surface diffusion of adsorbed molecules in porous media: Monolayer, multilayer, and capillary condensation regimes. Industrial & engineering chemistry research 40, 4005-4031.

Cihan, A., Tokunaga, T.K., Birkholzer, J.T., 2019. Adsorption and capillary condensation-induced imbibition in nanoporous media. Langmuir 35, 9611-9621.

Cihan, A., Tokunaga, T.K., Birkholzer, J.T., 2021. Diffusion‐to‐Imbibition Transition in Water Sorption in Nanoporous Media: Theoretical studies. Water Resources Research, e2021WR029720.

Clarke, D., Lawn, B., Roach, D., 1986. The role of surface forces in fracture, Fracture Mechanics of Ceramics. Springer, pp. 341-350.

Crichton, S.N., Tomozawa, M., Hayden, J.S., Suratwala, T.I., Campbell, J.H., 1999. Subcritical crack growth in a phosphate laser glass. Journal of the American Ceramic Society 82, 3097-3104.

Diao, Y., Espinosa-Marzal, R.M., 2016. Molecular insight into the nanoconfined calcite–solution interface. Proceedings of the National Academy of Sciences 113, 12047-12052.

Dziadkowiec, J., 2019. Interactions between Confined Calcite Surfaces in Aqueous Solutions: A surface forces apparatus study.

Dziadkowiec, J., Javadi, S., Bratvold, J.E., Nilsen, O., Røyne, A., 2018. Surface Forces Apparatus measurements of interactions between rough and reactive calcite surfaces. Langmuir 34, 7248-7263.

Dziadkowiec, J., Zareeipolgardani, B., Dysthe, D.K., Røyne, A., 2019. Nucleation in confinement generates long-range repulsion between rough calcite surfaces. Scientific reports 9, 1-15.

Eppes, M., Hancock, G., Chen, X., Arey, J., Dewers, T., Huettenmoser, J., Kiessling, S., Moser, F., Tannu, N., Weiserbs, B., 2018. Rates of subcritical cracking and long-term rock erosion. Geology 46, 951-954.

Eppes, M.C., Keanini, R., 2017. Mechanical weathering and rock erosion by climate‐dependent subcritical cracking. Reviews of Geophysics 55, 470-508.

Eskandari-Ghadi, M., Zhang, Y., 2021. Mechanics of shrinkage-swelling transition of microporous materials at the initial stage of adsorption. International Journal of Solids and Structures 222, 111041.

Eskandari-Ghadi, M., Zhang, Y., 2022. Modeling sorption-induced deformation of porous media: effect of pore size distribution. International Journal of Solids and Structures (Under Review).

Freiman, S.W., Wiederhorn, S.M., Mecholsky, J., John J, 2009. Environmentally enhanced fracture of glass: a historical perspective. Journal of the American Ceramic Society 92, 1371-1382.

Gdoutos, E.E., 2020. Fracture mechanics: an introduction. Springer Nature.

Hillerborg, A., Modéer, M., Petersson, P.-E., 1976. Analysis of crack formation and crack growth in concrete by means of fracture mechanics and finite elements. Cement and concrete research 6, 773-781.

Irwin, G.R., 1957. Analysis of stresses and strains near the end of a crack traversing a plate.

Israelachvili, J.N., 2011. Intermolecular and surface forces. Academic press.

Jennings, S., 1988. The mean free path in air. Journal of Aerosol Science 19, 159-166.

Karimpour, H., Lade, P.V., 2010. Time effects relate to crushing in sand. Journal of Geotechnical and Geoenvironmental Engineering 136, 1209-1219.

Kilburn, C.R., Voight, B., 1998. Slow rock fracture as eruption precursor at Soufriere Hills volcano, Montserrat. Geophysical Research Letters 25, 3665-3668.

Kim, J., Aluru, N., Tortorelli, D., 2003. Improved multi‐level Newton solvers for fully coupled multi‐physics problems. International journal for numerical methods in engineering 58, 463-480.

Lawn, B., 1974. Diffusion-controlled subcritical crack growth in the presence of a dilute gas environment. Materials Science and Engineering 13, 277-283.

Lawn, B.R., 1975. An atomistic model of kinetic crack growth in brittle solids. Journal of Materials Science 10, 469-480.

Lawn, B.R., 1985. Interfacial forces and the fundamental nature of brittle cracks. Applied physics letters 47, 809-811.

Le, J.-L., Bažant, Z.P., Bazant, M.Z., 2009. Subcritical crack growth law and its consequences for lifetime statistics and size effect of quasibrittle structures. Journal of Physics D: Applied Physics 42, 214008.

Lennartz-Sassinek, S., Main, I., Zaiser, M., Graham, C., 2014. Acceleration and localization of subcritical crack growth in a natural composite material. Physical Review E 90, 052401.

Li, D., Wei, D., 2020. Rate-Dependent Cohesive Zone Model for Fracture Simulation of Soda-Lime Glass Plate. Materials 13, 749.

MAI, Y.W., Lawn, B.R., 1987. Crack‐interface grain bridging as a fracture resistance mechanism in ceramics: II, Theoretical fracture mechanics model. Journal of the American Ceramic Society 70, 289-294.

Meng, F., Thouless, M., 2019. Cohesive-zone analyses with stochastic effects, illustrated by an example of kinetic crack growth. Journal of the Mechanics and Physics of Solids 132, 103686.

Meyland, M.J., Nielsen, J.H., Kocer, C., 2021. Tensile behaviour of soda-lime-silica glass and the significance of load duration–A literature review. Journal of Building Engineering, 102966.

Michalske, T.A., Freiman, S.W., 1982. A molecular interpretation of stress corrosion in silica. Nature 295, 511-512.

Nara, Y., Morimoto, K., Hiroyoshi, N., Yoneda, T., Kaneko, K., Benson, P.M., 2012. Influence of relative humidity on fracture toughness of rock: implications for subcritical crack growth. International Journal of Solids and Structures 49, 2471-2481.

Needleman, A., 1990. An analysis of tensile decohesion along an interface. Journal of the Mechanics and Physics of Solids 38, 289-324.

Nguyen, O., Repetto, E., Ortiz, M., Radovitzky, R., 2001. A cohesive model of fatigue crack growth. International Journal of Fracture 110, 351-369.

Olson, J.E., 1993. Joint pattern development: Effects of subcritical crack growth and mechanical crack interaction. Journal of Geophysical Research: Solid Earth 98, 12251-12265.

Planas, J., Elices, M., 1991. Nonlinear fracture of cohesive materials, Current trends in concrete fracture research. Springer, pp. 139-157.

Rice, J.R., 1978. Thermodynamics of the quasi-static growth of Griffith cracks. Journal of the Mechanics and Physics of Solids 26, 61–78.

Røyne, A., Dalby, K.N., Hassenkam, T., 2015. Repulsive hydration forces between calcite surfaces and their effect on the brittle strength of calcite‐bearing rocks. Geophysical Research Letters 42, 4786-4794.

Sills, R., Thouless, M., 2015. Cohesive-length scales for damage and toughening mechanisms. International Journal of Solids and Structures 55, 32-43.

Simmons, G.W., Pao, P., Wei, R., 1978. Fracture mechanics and surface chemistry studies of subcritical crack growth in AISI 4340 steel. Metallurgical Transactions A 9, 1147-1158.

Tada, H., 1972. Studies of the crack opening stretch concept in application to several fracture problems. Lehigh University.

Tada, H., Paris, P., Irwin, G., 2000. The analysis of cracks handbook. New York: ASME Press 2, 1.

Tijssens, M., Van der Giessen, E., Sluys, L., 2000. Modeling of crazing using a cohesive surface methodology. Mechanics of Materials 32, 19-35.

Tsilingiris, P., 2008. Thermophysical and transport properties of humid air at temperature range between 0 and 100 C. Energy Conversion and Management 49, 1098-1110.

Tvergaard, V., Hutchinson, J.W., 1992. The relation between crack growth resistance and fracture process parameters in elastic-plastic solids. Journal of the Mechanics and Physics of Solids 40, 1377-1397.

Wan, K.-T., Aimard, N., Lathabai, S., Horn, R.G., Lawn, B.R., 1990. Interfacial energy states of moisture-exposed cracks in mica. Journal of Materials Research 5, 172-182.

Wiederhorn, S., 1967. Influence of water vapor on crack propagation in soda ‐ lime glass. Journal of the American Ceramic Society 50, 407-414.

Wiederhorn, S., 1969. Fracture surface energy of glass. Journal of the American Ceramic Society 52, 99-105.

Wiederhorn, S., 1974. Subcritical crack growth in ceramics, Fracture mechanics of ceramics. Springer, pp. 613-646.

Wiederhorn, S., Bolz, L., 1970. Stress corrosion and static fatigue of glass. Journal of the American ceramic society 53, 543-548.

Wiederhorn, S., Fuller Jr, E., Thomson, R., 1980. Micromechanisms of crack growth in ceramics and glasses in corrosive environments.

Wiederhorn, S.M., Fuller Jr, E.R., 1989. Effect of surface forces on subcritical crack growth in glass. Journal of the American Ceramic Society 72, 248-251.

Wu, K., Li, X., Wang, C., Yu, W., Chen, Z., 2015. Model for surface diffusion of adsorbed gas in nanopores of shale gas reservoirs. Industrial & Engineering Chemistry Research 54, 3225-3236.

Xu, X., Xu, J., Chen, J., Li, P., Liu, B., Li, Y., 2017. Investigation of dynamic multi-cracking behavior in PVB laminated glass plates. International Journal of Impact Engineering 100, 62-74.

Yaminsky, V., Stewart, A., 2003. Interaction of glass surfaces in air: Dispersion forces in the retarded regime. Langmuir 19, 4037-4039.

Zhang, Y., Buscarnera, G., 2018. Breakage mechanics for granular materials in surface-reactive environments. Journal of the Mechanics and Physics of Solids 112, 89-108.

APPENDIX A. NUMERICAL SOLUTION TO THE Π-*W* SYSTEM

The solution to the $\Pi - w$ system involves finding a consistent set of $\Pi(x)$ and $w(x)$ that satisfy two equations of the general forms $w(x) = w(x, \Pi(x))$ and $\Pi(x) = \Pi(x, w(x))$. Eq. (2) is an example of the former, and Eqns. (9) and (10) take the form of the latter.

To write Eq. (2) in discrete form, an approximation for the integral on the right-hand side is required. Such approximation is commonly performed by adopting Gauss quadrature methods. However, due to the singularity of the fundamental solution, Eq. (4), at $x = s$, Gauss quadrature approximation encountered numerical convergence issues. Here an alternative approximation is adopted. Refer to the spatial discretization in Section 6. First, the disjoining pressure over the range of x_i and x_{i+1}, $\Pi_i^{elem}(x)$, is approximated with a constant value, $\Pi_i^{elem} = (\Pi(x_i) + \Pi(x_{i+1}))/2 = (\Pi_i + \Pi_{i+1})/2$. With this, Eqns. (1) and (2) can be written at each node as

$$w(x_i) = c_\sigma(x_i)\sigma + \sum_{j=1}^{N-1} \Pi_j^{elem} \underbrace{\int_{s=s_j}^{s=s_{j+1}} c_\Pi(x_i, s)ds}_{\mathbf{c}_\Pi^{elem}} \text{ and } K_{Ie} = k_{I\sigma}\sigma + \sum_{j=1}^{N-1} \Pi_j^{elem} \underbrace{\int_{s=s_j}^{s=s_{j+1}} k_{I\Pi}(s)ds}_{\mathbf{k}_{I\Pi}^{elem}} \qquad \text{(A.1)}$$

The fundamental functions $c_\Pi(x,s)$ and $k_{I\Pi}(s)$ are now the crack opening profile and the stress intensity factor for uniformly distributed stress over range (s_j, s_{j+1}) in Fig. A.1a, which are non-singular. For unit repulsive stress ($\Pi = 1$) applied over length s in Fig. A.1b, Tada (1972) provides

$$\int_0^s c_\Pi(x,s)ds = \frac{8(1-\nu^2)}{\pi E} \left\{ \begin{array}{l} \sqrt{a^2 - x^2} \sin^{-1}\dfrac{s}{a} + \dfrac{1}{2}|x-s|\cosh^{-1}\dfrac{a^2 - sx}{a|x-s|} \\ +\dfrac{1}{2}|x+s|\cosh^{-1}\dfrac{a^2 + sx}{a|x+s|} \end{array} \right\} \qquad \text{(A.2)}$$

$$\int_0^s k_{I\Pi}(s)ds = 2\sqrt{\frac{a}{\pi}} \sin^{-1}\frac{s}{a} \qquad \text{(A.3)}$$

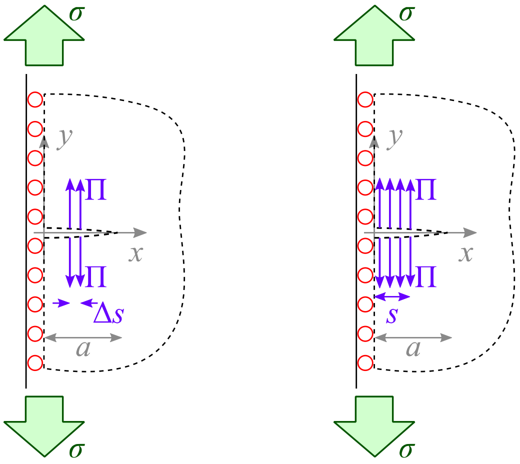

(a) (b)

Fig. A.1 Geometry considered in (a) this paper in deriving the fundamental solutions and (b) Tada (1972).

The fundamental solutions for uniform stress over an arbitrary segment (s_j, s_{j+1}) in the integrals of Eq. (A.1) can be directly expressed in terms of Eqns. (A.2) and (A.3), as

$$\int_{s=s_j}^{s=s_{j+1}} c_\Pi(x_i, s)ds = \int_0^{s_{j+1}} c_\Pi(x_i, s)ds - \int_0^{s_j} c_\Pi(x_i, s)ds \quad \text{and} \quad \int_{s=s_j}^{s=s_{j+1}} k_{I\Pi}(s)ds = \int_0^{s_{j+1}} k_{I\Pi}(s)ds - \int_0^{s_j} k_{I\Pi}(s)ds \quad .$$

$c_\sigma(x_i)$ and $k_{I\sigma}$ are given by Eq. (3). Eq. (A.1) can be written in a fully discretized form

$$w_i = c_{\sigma,i}\sigma + \sum_{j=1}^{N-1} c_{\Pi,ij}^{elem}\Pi_j^{elem} \quad \text{and} \quad K_{Ie} = k_{I\sigma}\sigma + \sum_{j=1}^{N-1} k_{I\Pi,j}^{elem}\Pi_j^{elem} \tag{A.4}$$

where $c_{\sigma,i} = c_\sigma(x_i)$. $\Pi_i^{elem} = (\Pi_i + \Pi_{i+1})/2$ can also be written as a tensor transformation, $\mathbf{\Pi}^{elem} = \mathbf{A}_\Pi \cdot \mathbf{\Pi}$, where

$$\mathbf{A}_\Pi = \begin{bmatrix} \tfrac{1}{2} & \tfrac{1}{2} & 0 & 0 & & 0 & 0 \\ 0 & \tfrac{1}{2} & \tfrac{1}{2} & 0 & \cdots & 0 & 0 \\ 0 & 0 & \tfrac{1}{2} & \tfrac{1}{2} & & 0 & 0 \\ & \vdots & & & \ddots & 0 & 0 \\ 0 & 0 & 0 & 0 & 0 & \tfrac{1}{2} & \tfrac{1}{2} \end{bmatrix}_{(N-1)\times N} \tag{A.5}$$

Finally, Eq. (A.4) can be written in matrix-vector notation as:

$$\mathbf{w} = \mathbf{c}_\sigma \sigma + \mathbf{c}_\Pi \cdot \mathbf{\Pi} \tag{A.6}$$

$$K_{Ie} = k_{I\sigma}\sigma + \mathbf{k}_{I\Pi} \cdot \mathbf{\Pi} \tag{A.7}$$

where $\mathbf{c}_{\Pi} = \mathbf{c}_{\Pi}^{elem} \cdot \mathbf{A}_{\Pi}$ and $\mathbf{k}_{I\Pi} = \left(\mathbf{k}_{I\Pi}^{elem}\right)^{T} \cdot \mathbf{A}_{\Pi}$. Substituting the relation $\Pi = \Pi(w, p)$ into Eq. (A.6) yields a nonlinear algebraic equation that can be solved iteratively. The solution is sought here by rewriting Eq. (A.6) in the same way as Planas and Elices (1991):

$$\mathbf{\Pi}(\mathbf{w},\mathbf{p}) - \mathbf{M} \cdot \mathbf{w} + \mathbf{L}\sigma = \mathbf{0} \tag{A.8}$$

where $\mathbf{p}$ is the nodal vector of gas partial pressure assumed to be known and constant in this local solver, $\mathbf{M} = \mathbf{c}_{\Pi}^{-1}$, and $\mathbf{L} = \mathbf{c}_{\Pi}^{-1} \cdot \mathbf{c}_{\sigma}$. A Newton-Raphson iteration method is implemented to seek the solution w_i at each node. Starting with an initial guess, $\mathbf{w}_0$, the correction $\mathbf{w}_{k+1} = \mathbf{w}_k + \delta\mathbf{w}_k$ at iteration k is made where $\delta\mathbf{w}_k = -(\mathbf{J}^M)^{-1} \cdot \mathbf{R}^M$. $\mathbf{R}^M$ and $\mathbf{J}^M$ are computed as

$$R_i^M = \Pi(w_i, p_i) - M_{ij} w_j + L_i \sigma \text{ and } J_{ij}^M = \left.\frac{\partial \Pi}{\partial w}\right|_{w_i, p_i} \delta_{ij} - M_{ij} \tag{A.9}$$

with $\mathbf{w} = \mathbf{w}_k$. The search for solution continues until the error defined as

$$\varepsilon_M = \sqrt{\sum_{1}^{N-1} (R_i^M)^2 \Delta x_i} \tag{A.10}$$

is reduced below a tolerance (here taken as 5×10^{-4}). Once Π and w profiles are obtained, Eq. (A.7) computes K_{Ie} to conclude the $\Pi - w$ system solver.

Our $\Pi - w$ system solver is verified by comparing the computed crack opening profile with the analytical crack opening solutions of Tada et al. (2000) subjected to different surface force distributions (Fig. A.2).

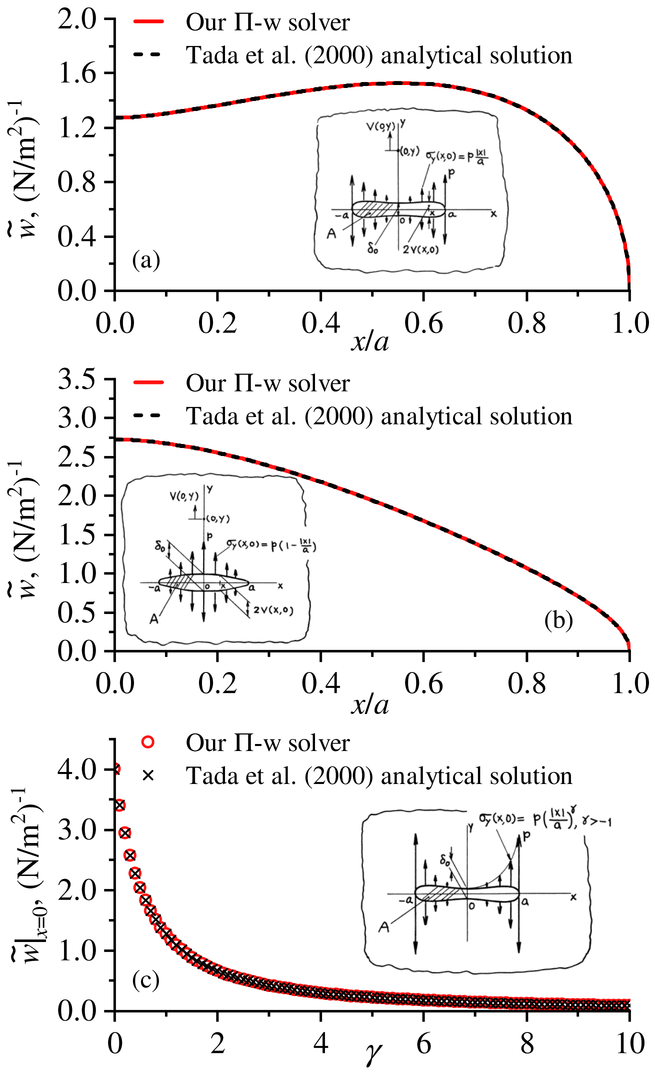

Fig. A.2 Verification of the normalized crack opening profile, $\tilde{w} = wE/(1-\nu^2)a$, with exact solutions (Tada et al., 2000) for surface force distributions (a) linearly increasing toward the crack tip; (b) linearly decreasing toward the crack tip; and (c) nonlinearly increasing toward the crack tip. Figure insets are courtesy of Tada et al. (2000).

APPENDIX B. INITIAL GUESS FOR $T > 0$ AND $T = 0$

The current implementation is stress-controlled (i.e., σ and a vary between timesteps). The crack velocity is small and the timesteps are close, thus the variation of a over timesteps is very small. However, a small variation in σ can create a large change in K_{Ie} which exponentially updates v_c and subsequently $p(x)$. It is thus apparent that using the solution at timestep t_k as the initial guess for timestep t_{k+1} can involve large errors and prevent convergence.

We can obtain an initial guess for timestep t_{k+1} by a linear extrapolation. The rate of change of the solution vector, $\mathbf{u}$, over time Δt is linearized based on a small variation of σ over a small time . $\theta\Delta t$. as

$$\frac{\Delta \mathbf{u}}{\Delta t} \approx \frac{\mathbf{u}\,|_{\sigma(t_k+\theta\Delta t)} - \mathbf{u}\,|_{\sigma(t_k)}}{\theta\Delta t} \tag{B.1}$$

The value of θ is set to 10^{-2}. Since the variation of σ over the time interval $\theta\Delta t$ is now small, the solution at time t_k works as a good initial guess for the solution at time $t_k + \theta\Delta t$. Thus, $\mathbf{u}\,|_{\sigma(t_k+\theta\Delta t)}$ is found using the same partitioned Newton-Raphson solver with the initial guess of $\mathbf{u}\,|_{\sigma(t_k)}$. The sole purpose of $\mathbf{u}\,|_{\sigma(t_k+\theta\Delta t)}$ is to assist with finding a reasonable initial guess for $\mathbf{u}\,|_{\sigma(t_k+\Delta t)}$, it can thus be calculated with a more relaxed tolerance to reduce simulation time. Then, the initial guess for time t_{k+1} is computed via linear extrapolation:

$$\mathbf{u}\,|_{\sigma(t_k+\Delta t)} \approx \mathbf{u}\,|_{\sigma(t_k)} + \frac{\Delta \mathbf{u}}{\Delta t}\Delta t \tag{B.2}$$

While the procedure described here involves an additional set of iterations in search of $\mathbf{u}\,|_{\sigma(t_k+\theta\Delta t)}$, the amount of computation required for those iterations is far less than that required for finding the solution to $\mathbf{u}\,|_{\sigma(t_k+\Delta t)}$ using the initial guess $\mathbf{u}\,|_{\sigma(t_k)}$ even if the latter converges.

The initial guess for $t = 0$ can be obtained by starting simulations with a small σ so that v_c can be predicted a few orders of magnitude smaller than d / D. This way, the fluid profile is known, $p(x) = p_0$. Thus, the $\Pi - w$ system can be solved alone for K_{Ie}. One must then verify that this K_{Ie} results in v_c of similar magnitude as the predicted one.